A MAPPING-VARIABLE RING POLYMER MOLECULAR DYNAMICS STUDY OF MULTI-STATE REACTION MECHANISMS IN THE CONDENSED PHASE

A Dissertation

Presented to the Faculty of the Graduate School

of Cornell University

in Partial Fulfillment of the Requirements for the Degree of

Doctor of Philosophy

by

Sadrach Pierre

May 2018

A MAPPING-VARIABLE RING POLYMER MOLECULAR DYNAMICS STUDY OF MULTI-STATE REACTION MECHANISMS IN THE CONDENSED PHASE

Sadrach Pierre, Ph.D.

Cornell University 2018

The accurate description of the coupled nuclear and electronic motion in large complex systems is necessary to inform the design of renewable energy devices. Treating many-body systems with exact quantum dynamics is typically intractable due to the exponential scaling of quantum mechanics. It is therefore of theoretical interest to develop accurate approximate quantum dynamics methods that are able to capture the mechanisms and varying time scales of many-body systems, while retaining the favorable linear scaling of classical methods. The focus of this dissertation is the development and application of an approximate quantum dynamics method towards elucidating mechanisms in the condensed phase.

The approximate quantum dynamic method of interest is based on the path integral representation of the quantum Boltzmann distribution [1]. The quantum Boltzmann distribution describes the classical distribution of a "ring polymer" in an extended phase space. Mapping Variable RPMD (MV-RPMD) is an extension of RPMD that allows for the classical treatment of electronic state transitions by mapping discrete states to continuous phase-space variables and it employs classical trajectories to calculate real-time thermal correlation functions [2]. We study the condensed phase reaction dynamics of a proton-coupled electron transfer (PCET) system and an electron transfer (ET) system using MV-

RPMD.

We derive a more numerically stable quantum Boltzmann distribution in the MV-RPMD framework by invoking the symmetric Trotter approximation. We construct a four-state electron-proton system from a model PCET system bath model comprised of a proton double well coupled to two discrete electronic states. We establish bead convergence with significantly fewer beads than required in the original system. Further, in studying the mechanism of PCET we show that population dynamics generated from MV-RPMD trajectories can be used to accurately distinguish concerted and sequential PCET mechanisms. We verify the accuracy of PCET mechanisms predicted by MV-RPMD population dynamics by comparing against Fermi's Golden Rule and Kramers rate calculations.

It is known that RPMD is an approximation to the "ImF" version of semiclassical instanton theory when used to calculate reaction rates in the deep tunneling regime [3]. This speaks to RPMD's accuracy in approximating reaction rates within this regime. In an effort to develop a nonadiabatic rate theory in the MV-RPMD framework, we apply the method towards the calculation of an MV-RPMD instanton configuration in a model two-state system [4] and provide preliminary results. Knowledge of the MV-RPMD instanton can provide transition state information necessary for a nonadiabatic rate calculation. In this vein, following our instanton configuration calculations, we develop three new rate expressions, in terms of flux-side thermal correlation functions(TCF), in the MV-RPMD framework .

BIOGRAPHICAL SKETCH

Hailing from Flatbush, Brooklyn, Sadrach cultivated his interests in the natural and physical sciences at Midwood High School. While attending Midwood, Sadrach participated in the Intel Science club which allowed him to join an Organic Chemistry Lab, in the Gough Group, at Long Island University during his Junior year of High School. Sadrach continued on his scientific journey by accepting a full-tuition scholarship through the Brandeis University Science Posse scholarship program. At Brandeis, Sadrach majored in Chemistry, and minored in applied mathematics. Sadrach's interests in research continued to develop as he took on an inorganic renewable energy materials project in the Thomas Group which eventually became his Honors thesis. After numerous experiences in undergraduate research at Brandeis, as well as during internships in plant immunology, drug discovery, and sustainable energy Sadrach found his interests residing in the field of chemical physics which lead him pursue his doctoral degree at Cornell University. As a National Defense Science and Engineering Graduate Fellow, he has spent his time developing novel mathematical methods used to inform the design of rational renewable energy devices. In his spare time, Sadrach enjoys reading Modern and Contemporary fiction (Gaddis, Mann, Pynchon, DFW), American History nonfiction (American Revolution and Civil War), and taking on interesting machine learning projects (support vectors, kernels, clustering).

For my mom, my sister and Ruth: Without your support this would not be possible.

ACKNOWLEDGEMENTS

Several individuals, including professors, family, friends and mentors, have provided unwavering support throughout my graduate career, without which the completion of this thesis would not be possible.

First I would like to thank my advisor, Professor Nandini Ananth. Thank you for your unfettered patience and pedagogy which has allowed me to develop into an independent scientist and a valuable member of the scientific community. Thank you for the emotional support you provided during some of the toughest moments of my graduate career. Your kindness, patience and loyalty to mentorship did not go unnoticed.

I would also like to thank the faculty of the Chemistry Department. Specifically, I would like to thank my thesis committee Professor Roger Loring, and Professor Poul Petersen for their guidance throughout my graduate career. Further, I would like to thank Professor Greg Ezra and Professor John Marohn for their mentorship and the many interesting scientific and non-scientific conversations we've had.

I would also like to thank one of my most impactful mentors outside of my professional career, Rabbi Jeremy Fierstein. The countless conversations we've had about Judaism and Jewish practice have significantly shaped my worldview and personal values. I truly wouldn't have been able to complete this work without your emotional support and mentorship. I would also like to thank the late Professor Alfred Phillips Jr. (former Cornell Electrical Engineering Professor). You were the only academic professional I knew who looked like me, which held significant weight in a world where "successful" African American men were too frequently alone. Thank you for your conversations covering a broad range of topics including, Feynman Path Integrals, quantum field the-

ory, string theory, classic literature, and race in America. Your knowledge and advice has been invaluable and has largely contributed to my personal growth. I would also like to thank Marquis Bey (currently a PhD candidate in English at Cornell). Our conversations about hegemonic race and gender constructs have greatly contributed to my worldview and provided much groundwork for how I've come to understand myself today.

I appreciate the support and love of my family. To my mom, thank you for your unending support and your uncanny ability to keep me stabilize me during tough social and professional times. To Edwidge, thank you for being a major support system for me over the past five years. You are an amazing mother and sister. I hope you know you are appreciated and your staunch loyalty, unconditional love and emotional resilience are acknowledged. To Peniel, growing up you always called me "Mr. Scientist" (albeit, sarcastically, during moments I didn't deserve the title). Thank you for being such a great big brother. You are more inspiring to me than you realize. I hope this dissertation makes you proud enough to soberly call me "Mr. Scientist".

I would also like to thank Ruth Zeilicovich. I can't thank you enough for your friendship, love and support. You've kept me grounded and focused. You are an inspiration to me in so many ways and continue to help me grow as a person. I hope this work makes you proud.

I would also like to thank my coworkers. You have all been invaluable peers and friends. Specifically, Tim thank you for your unconditional intellectual guidance, inspirational allegiance to scholarship, witty humor, and your cognizant politics. You are a paragon of intellectualism. Thank you to Elliot for being my dashboard for bad jokes and popular culture. Just remember, you've got to FOLLOW THE RULES. Thank you to Matt for fun times spent in and

outside of lab. You have served as my ”Jim” from ”The Office” (I’m probably Darryl or Ryan). Your service is now complete and you can be Matt once again if you so wish. To Britta, while we’ve only known each other a few months we’ve come to be good friends for which I am thankful. I’ll miss our walks and marathon sessions of ”Parks and Recreation .” Last but not least, thank you to my niece Madison Jarrells. I love you and I hope this work inspires you to go on and do great things.

The work described in this dissertation was funded by a NDSEG Fellowship (FA9550-11-C-0028) awarded by the Department of Defense, Air Force Office of Scientific Research, a National Science Foundation CAREER Award (No. CHE-1555205), an Alfred P. Sloan Foundation Fellowship, and a Cottrell Scholar Award.

TABLE OF CONTENTS

LIST OF TABLES

LIST OF FIGURES

CHAPTER 1

INTRODUCTION

Charge and energy transfer in the condensed phase mediate many natural processes including the tyrosine oxidation step in photosynthesis [5, 6, 7, 8], the proton pumping mechanism in respiration and emerging renewable energy technologies such as organic photovoltaics and dye-sensitized solar cells [9, 10]. Further understanding of the mechanisms underlying these processes will inform the design of more efficient clean energy technologies. However, statistical methods are useful for determining energy landscapes, equilibrium properties such as average energy, and statistical distributions of nuclei. Statistical methods fail to provide information about reactive pathways in chemical systems. Experimental studies provide information about long-time dynamics but fail to give short time information.

Real-time quantum dynamics methods can probe subfemtosecond dynamics but are only feasible in small systems due to the exponential scaling problem in quantum mechanics [11]. Additionally, accurately describing the wide range of time scales and the degree of coupling between light and heavy quantum mechanical particles in large complex systems remains a theoretical challenge. While molecular dynamics is ideal because it scales linearly with system size, it fails to capture quantum mechanical properties such as tunneling, zero-point energy (ZPE) and interference.

Several approximations to quantum dynamics in large complex systems have been reported in the literature. For example mixed quantum/classical (MQC) methods such as surface hopping have been used to study systems such as proton transfer, PCET, and ET [7, 12, 13]. MQC methods typically treat

heavy nuclei classically and electronic degrees of freedom quantum mechanically. While these methods are tractable relative to exact quantum dynamics, they fail to preserve thermal distributions and accurately describe population dynamics in the condensed phase due to the inconsistent treatment of coupled nuclear and electronic motion. MQC methods consequently suffer from uncontrolled approximations to the coupled electronic and nuclear motion. More accurate methods that introduce semiclassical approximations to quantum dynamics, treat all degrees of freedom in a consistent framework but lack efficiency and fail to preserve detailed balance.

Approximate quantum dynamics methods also include a path integral based methods based on the discretization of the quantum Boltzmann distribution (QBD). These imaginary-time PI methods are favorable because they employ classical trajectories and consequently scale almost linearly with system size. Further, these methods treat all degrees of freedom in a consistent dynamic framework, incorporate quantum tunneling and ZPE, and preserve the QBD.

Ring polymer molecular dynamics (RPMD) is an accurate and efficient method for short-time dynamics including charge and energy transfer in large complex systems. RPMD's linear scaling, preservation of the QBD, its consistent treatment of degrees of freedom, and its accurate description of tunneling and ZPE [14] has made it a viable method for studying a wide range of chemical processes in the condensed phase. For example RPMD has been used to simulate quantum diffusion in liquid water, quantum diffusion in para-hydrogen [15], hydride transfer rates in enzymes [16], bimolecular reaction rates [17, 18], mixed valence ET in water between iron atoms [19], ET between cobalt hexamine complexes in water [20] and several other applications. A shortcoming

of RPMD is in its treatment of electrons as distinguishable particles which limits its applicability to single electron processes. Further, RPMD does not allow for the simulation of nonadiabatic processes, where the coupled motion of electrons and nuclei occur on similar timescales.

It is of theoretical interest to develop extensions of RPMD which account for the indistinguishable nature of electrons while also allowing for the treatment of nonadiabatic processes. Several nonadiabatic versions of RPMD have been reported in the literature, including surface hopping RPMD [21], Kinetically constrained RPMD (KC-RPMD) [22], Coherent state RPMD [23], nonadiabatic MF-RPMD [24] and more [25, 2, 26, 27]. While there are several RPMD extensions reported in the literature, the focus in the dissertation will be on developing and applying MV-RPMD [27, 2]. This extension, which originated in our group, employs continuous electronic and nuclear variables which can be used to generate classical equations of motion [2]. This method has been used to simulate photo-initiated dynamics in model three-state systems in the gas phase [27]. In an effort to extend MV-RPMD's utility towards larger and more realistic systems, we employ MV-RPMD in the simulation of condensed phase nonadiabatic dynamics. The first application will be in studying the chronology of proton and electron transfer in model PCET systems [28]. Further, in the interest of applying MV-RPMD to a wider range of chemical problems we perform instanton configuration calculations. These calculations provide insight into how, within the MV-RPMD framework, we can undertake a rate calculation in a model ET system in the condensed phase.

We start off the discussion with a review of the original RPMD formulation. In chapter 2 we go into detail about its advantages and limitations. We then

discuss the nonadiabatic extension of RPMD, MV-RPMD, and the derivation of a classically isomorphic QBD which generates statistics with increased stability. In chapter 3 we discuss various PCET models that have been reported in the literature. In chapter 4 we use MV-RPMD to gain mechanistic insight in model PCET systems. In chapter 5 we review semiclassical instanton theory and provide preliminary results for instanton configuration calculations for a model two-state system. In chapter 5 we review RPMD rate theory, provide the framework for its extension to nonadiabatic rate calculations in the MV-RPMD framework, and outline the formalism for three novel MV-RPMD rate theories. In chapter 6 we summarize our results and provide direction for future studies.

CHAPTER 2

IMAGINARY-TIME PATH INTEGRALS

In this section we will discuss the path integral discretization of the QBD. We will discuss the RPMD approximation, its range of accuracy and some of the limitations that have inspired its extended forms.

The exponential scaling of configuration space in quantum mechanics renders directly solving the Schrödinger equation for large, complex and often more interesting systems an intractable challenge [29, 30]. One method for circumventing the exponential scaling of computational cost for quantum systems is to take advantage of the classical isomorphism between the equilibrium statistics of a quantum particle and the classical statistics of a ring polymer. This allows us to reconstitute a quantum problem into a linearly scaled classical problem. We start by considering a general system with mass M, momentum P and coordinate R moving in a general one dimensional potential $V(R)$ described by the Hamiltonian,

$$\hat{H} = \frac{\hat{P}^2}{2M} + V(\hat{R}) = \hat{T} + \hat{V}. \tag{2.1}$$

The canonical partition function for a system with Hamiltonian, H, can be written as the trace over the Boltzmann operator,

$$Z = Tr[e^{-\beta\hat{H}}] = Tr[e^{-\beta(\hat{T}+\hat{V})}] \tag{2.2}$$

where β is $1/k_bT$ and T is the system temperature. The trace can be written in the basis of system coordinates as

$$Z = Tr[e^{-\beta(\hat{T}+\hat{V})}] = \int dR \langle R|e^{-\beta(\hat{T}+\hat{V})}|R\rangle. \tag{2.3}$$

Since $\hat{T}$ and $\hat{V}$ do not commute we employ the Trotter approximation and write the trace as,

$$Z = \int dR \langle R|e^{-\beta(\hat{T}+\hat{V})}|R\rangle = \lim_{P\to\infty} \int dR \langle R|(e^{-\frac{\beta}{2P}\hat{V}} e^{-\frac{\beta}{P}\hat{T}} e^{-\frac{\beta}{2P}\hat{V}})^P|R\rangle. \tag{2.4}$$

We then insert $P-1$ copies of identity

$$I = \int dR|R\rangle\langle R| \tag{2.5}$$

and we obtain a product of matrices

$$\begin{aligned} Z = \lim_{P\to\infty} \int d\{R_\alpha\} &\langle R_1|e^{-\frac{\beta}{2P}\hat{V}} e^{-\frac{\beta}{P}\hat{T}} e^{-\frac{\beta}{2P}\hat{V}}|R_2\rangle\langle R_2|e^{-\frac{\beta}{2P}\hat{V}} e^{-\frac{\beta}{P}\hat{T}} e^{-\frac{\beta}{2P}\hat{V}}|R_3\rangle \\ \times &\langle R_3|\ldots|R_P\rangle\langle R_P|e^{-\frac{\beta}{2P}\hat{V}} e^{-\frac{\beta}{P}\hat{T}} e^{-\frac{\beta}{2P}\hat{V}}|R_1\rangle. \end{aligned} \tag{2.6}$$

We can then write,

$$\begin{aligned} Z &= \lim_{P\to\infty} \int d\{R_\alpha\} \prod_{\alpha=1}^{P} \langle R_\alpha|e^{-\frac{\beta}{2P}\hat{V}} e^{-\frac{\beta}{P}\hat{T}} e^{-\frac{\beta}{2P}\hat{V}}|R_{\alpha+1}\rangle \\ &= \lim_{P\to\infty} \int d\{R_\alpha\} \prod_{\alpha=1}^{P} \langle R_\alpha|e^{-\frac{\beta}{2P}\hat{V}} e^{-\frac{\beta}{P}\hat{T}} e^{-\frac{\beta}{2P}\hat{V}}|R_{\alpha+1}\rangle \end{aligned} \tag{2.7}$$

where $\{R_\alpha\} = \{R_1 \ldots R_P\}$. Evaluating the coordinate space matrix elements we get,

$$\langle R_\alpha|e^{-\frac{\beta}{2P}\hat{V}} e^{-\frac{\beta}{P}\hat{T}} e^{-\frac{\beta}{2P}\hat{V}}|R_{\alpha+1}\rangle = e^{-\frac{\beta}{2P}V(R_\alpha)} \langle R_\alpha|e^{-\frac{\beta}{P}\hat{T}}|R_{\alpha+1}\rangle e^{-\frac{\beta}{2P}V(R_{\alpha+1})}. \tag{2.8}$$

The matrix elements of the kinetic energy operator, $\langle R_\alpha|e^{-\frac{\beta}{P}\hat{T}}|R_{\alpha+1}\rangle$, can be evaluated by introducing a complete set of momentum states,

$$I = \int dp|p\rangle\langle p| \tag{2.9}$$

Where we now have

$$\int dP \langle R_\alpha|e^{-\frac{\beta}{P}\hat{T}}|p\rangle\langle p|R_{\alpha+1}\rangle = \int dp e^{-\frac{\beta}{2PM}p^2} \langle R_\alpha|p\rangle\langle P|R_{\alpha+1}\rangle. \tag{2.10}$$

The definition of the inner product of coordinate and momentum eigenstates is,

$$\langle R|p\rangle = \frac{1}{\sqrt{2\pi\hbar}} e^{ipR}. \tag{2.11}$$

The integral over momentum can be written as

$$\int dp e^{-\frac{\beta}{2PM}p^2}\langle R_\alpha|p\rangle\langle p|R_{\alpha+1}\rangle = \int dp e^{-\frac{\beta}{2PM}p^2} e^{(ipR_\alpha - ipR_{\alpha+1})}. \tag{2.12}$$

Upon completing the square and evaluating the momentum integral we obtain the matrix elements,

$$\begin{aligned}&\langle R_\alpha|e^{-\frac{\beta}{2P}\hat{V}}e^{-\frac{\beta}{P}\hat{T}}e^{-\frac{\beta}{2P}\hat{V}}|R_{\alpha+1}\rangle \\ &= \left(\frac{mP}{2\pi\beta\hbar^2}\right)^{1/2}\exp\Big[-\frac{mP}{2\beta\hbar^2}(R_\alpha - R_{\alpha+1})^2 - \frac{\beta}{2P}(V(R_\alpha)+V(R_{\alpha+1}))\Big].\end{aligned} \tag{2.13}$$

Due to the cyclic permutability of the trace, $R_{P+1} = R_1$, we have

$$\frac{\beta}{2P}(V(R_\alpha)+V(R_{\alpha+1})) = \frac{\beta}{P}V(R_\alpha). \tag{2.14}$$

Substituting this back into the equation for the partition function,

$$Z = \lim_{P\to\infty}\left(\frac{mP}{2\pi\beta\hbar^2}\right)^{P/2}\int d\{R_\alpha\}\exp\Big(-\sum_{\alpha=1}^{P}\Big[-\frac{mP}{2\beta\hbar^2}(R_\alpha - R_{\alpha+1})^2 - \frac{\beta}{P}(V(R_\alpha))\Big]\Big), \tag{2.15}$$

which is the exact expression for the QBD in that path integral framework. For a system with d nuclear dimensions, where $H = \frac{\hat{\mathbf{p}}^2}{2M} + V(\hat{\mathbf{R}})$ and $\hat{\mathbf{p}}$ and $\hat{\mathbf{R}}$ are vectors of d-dimensions the QBD is,

$$Z = \lim_{P\to\infty}\left(\frac{mP}{2\pi\beta\hbar^2}\right)^{dP/2}\int d\{\mathbf{R}_\alpha\}\exp\Big(-\sum_{\alpha=1}^{P}\Big[-\frac{mP}{2\beta\hbar^2}(\mathbf{R}_\alpha-\mathbf{R}_{\alpha+1})^T\cdot(\mathbf{R}_\alpha-\mathbf{R}_{\alpha+1}) - \frac{\beta}{P}(V(\mathbf{R}_\alpha))\Big]\Big). \tag{2.16}$$

We can connect the above expression to the quantum partition function by introducing a set of P normalized gaussian integrals,

$$I_N = \left(\frac{2\pi M'}{\beta_P}\right)^{dP/2}\int d\{\mathbf{p}_\alpha\}e^{-\frac{\beta_P}{2M}\sum_{\alpha=1}^{P}\mathbf{p}^T\cdot\mathbf{p}}. \tag{2.17}$$

The P-bead approximation to the quantum partition function is

$$Z = \lim_{P\to\infty}\int d\{\mathbf{p}_\alpha\}\int d\{\mathbf{R}_\alpha\}e^{-\beta_P H_P(\mathbf{R}_\alpha,\mathbf{p}_\alpha)} \tag{2.18}$$

where $\beta_P = \beta/P$ and

$$H_P = \sum_{\alpha=1}^{P} \left[\frac{\mathbf{p}_\alpha^T \cdot \mathbf{p}_\alpha}{2M} + \frac{mP^2}{2\beta^2\hbar^2} (\mathbf{R}_\alpha + \mathbf{R}_{\alpha+1})^T \cdot (\mathbf{R}_\alpha - \mathbf{R}_{\alpha+1}) + V(\mathbf{R}_\alpha) \right]. \tag{2.19}$$

The Gaussian variables are fictitious classical momenta, where the constant M' has units of mass. Since the Gaussian integrals are normalized we have freedom in our choice of M'. The representation of the exact quantum partition function as a P-dimensional classical phase-space integral for the fictitious classical system consisting of P bead is known as the classical isomorphism. This is also referred to as the P-bead imaginary-time path integral representation for the QBD. We can see this by considering the relationship $\beta/P = it/\hbar$. Solving for temperature we find $\beta = itP/\hbar$ and $T = \hbar/Pk_b it$. We can then interpret the fictitious beads in the ring polymer to be a slice in imaginary-time and the ring polymer to be imaginary-time propagation ($0 < t < \beta/P$).We arrive at an exact representation of the QBD as a product of matrix elements which is formally known to be the "path integral discretization." This idea originates from Feynman's use of path integrals in order to represent the quantum time evolution of a system with classical paths [31, 32, 33, 34]. Path integral molecular dynamics (PIMD) uses the classical dynamics generated by the Hamiltonian, H_P in Eq. (2.19) to sample the extended ring polymer phase space configurations along thermostatted trajectories and calculates exact quantum statistics in the limit of a large bead number P.

$$\dot{\mathbf{R}}_\alpha = \frac{\partial H_P}{\partial \mathbf{p}_\alpha}, \ \dot{\mathbf{p}}_\alpha = -\frac{\partial H_P}{\partial \mathbf{R}_\alpha} \tag{2.20}$$

Additionally, it is straightforward to use path integral Monte Carlo (PIMC) importance sampling in order to calculate exact quantum statistics within this framework. In this vein, exact quantum statistics can be calculated using the Boltzmann factor, $e^{-\beta_P H(\{\mathbf{R}_\alpha, \mathbf{P}_\alpha\})}$, to importance sample extended ring polymer

phase space configurations. Both PIMD and PIMC are very efficient for systems containing containing hundreds, sometimes thousands, of atoms. If we wish to compute the expectation value of a quantum mechanical operator $\hat{A}$, that is purely a function of the operator $\hat{R}$, such that $\hat{A} = A(\hat{R})$ we can write,

$$\langle \hat{A} \rangle = \frac{\mathrm{tr}[e^{-\beta \hat{H}} \hat{A}]}{\mathrm{tr}[e^{-\beta \hat{H}}]} = \frac{1}{Z} \mathrm{tr}[e^{-\beta \hat{H}} \hat{A}]. \tag{2.21}$$

We can write the expectation value in the limit of a discrete path integral as

$$\langle \hat{A} \rangle = \lim_{P \to \infty} \int d\{\mathbf{p}_\alpha\} \int d\{\mathbf{R}_\alpha\} \frac{1}{P} \sum_{\alpha=1}^{P} A(\mathbf{R}_\alpha) e^{-\beta_P H_P(\mathbf{R}_\alpha, \mathbf{p}_\alpha)} \tag{2.22}$$

where we define the quantity

$$A_P(\mathbf{R}_1 \ldots \mathbf{R}_P) = \frac{1}{P} \sum_{\alpha=1}^{P} A(\mathbf{R}_\alpha) \tag{2.23}$$

as the estimator for operator $\hat{A}$. In the limit of a large bead number the statistical average of the estimator will give the exact expectation value for the observable such that,

$$\langle A \rangle = \lim_{P \to \infty} \langle A_P(\mathbf{R}_1 \ldots \mathbf{R}_P) \rangle_{e^{-\beta H_P}}, \tag{2.24}$$

Where $\langle \ldots \rangle_{e^{-\beta H_P}}$ indicates the ensemble average is obtained with respect to the sampling function $e^{-\beta H_P}$. Thermodynamic quantities can be calculated within the path integral formalism. For example, consider the average internal energy given by,

$$E = -\frac{1}{Z} \frac{\partial}{\partial \beta} \ln Z = -\frac{1}{Z} \frac{\partial Z}{\partial \beta}. \tag{2.25}$$

The exact quantum mechanical expectation value of energy can be computed using path integrals,

$$\langle E \rangle = \lim_{P \to \infty} \langle E_P(\mathbf{R}_1 \ldots \mathbf{R}_P) \rangle_{e^{-\beta H_P}} \tag{2.26}$$

where the energy estimator is,

$$E_P(\mathbf{R}_1 \ldots \mathbf{R}_P) = \frac{P}{2\beta} - \sum_{\alpha=1}^{P} \left[\frac{MP}{2\beta^2 \hbar^2} (\mathbf{R}_\alpha - \mathbf{R}_{\alpha+1})^T \cdot (\mathbf{R}_\alpha - \mathbf{R}_{\alpha+1}) - \frac{1}{P} V(\mathbf{R}_\alpha) \right]. \tag{2.27}$$

2.1 RPMD Approximation

While the path integral discretization of the QBD lends a convenient and efficient route to generating exact quantum statistics, methods like PIMD and PIMC are limited to time-independent system properties. For more interesting processes such as charge and energy transfer in biological systems or energy technologies we need to employ dynamics methods. Ideally we would like a method that incorporates accurate quantum information while preserving the scalability of a classical dynamics method. To see how RPMD is a viable option we start by considering the real-time quantum correlation function for a system in thermal equilibrium,

$$c_{AB}(t) = \frac{1}{Q}\mathrm{Tr}[e^{-\beta\hat{H}}\hat{A}(0)\hat{B}(t)], \tag{2.28}$$

where $\hat{A}$ and $\hat{B}$ are Heisenberg-evolved system observables. Alternatively, this can be written in a more symmetric and thus more classical form as the Kubo-transformed correlation function,

$$\tilde{c}_{AB}(t) = \frac{1}{\beta Q}\int_0^\beta \mathrm{tr}[e^{-(\beta-\lambda)\hat{H}}\hat{A}(0)e^{-\lambda\hat{H}}\hat{B}(t)]d\lambda \tag{2.29}$$

where the Boltzmann operator $e^{-\beta\hat{H}}$ is symmetrically averaged between $\hat{A}(0)$. The Fourier transform of the quantum mechanical real-time correlation function and the Kubo-transformed correlation function are,

$$C_{AB}(\omega) = \int_{-\infty}^{\infty} e^{-i\omega t}c_{AB}(t)dt, \quad \tilde{C}_{AB}(\omega) = \int_{-\infty}^{\infty} e^{-i\omega t}\tilde{c}_{AB}(t)dt \tag{2.30}$$

and they have the relationship,

$$C_{AB}(\omega) = \frac{\beta\hbar\omega}{1-e^{-\beta\hbar\omega}}\tilde{C}_{AB}(\omega) \tag{2.31}$$

so knowledge of either is sufficient to calculate the other. The rigorous path integral discretization of Eq. (2.28) or Eq. (2.29) [31] can be done in a variety of

ways and leads to a number of exact and approximate methods for generating quantum dynamics. These include methods such as Quasi-adiabatic Path Integral (QUAPI) method [35, 30] and General Quantum Master Equations (GQME) [36, 37]. These methods tend to be highly demanding computationally and consequently impractical for large, often more interesting, systems. The reasoning behind the development of RPMD is to exploit the classical isomorphism between ring polymer statistics and quantum statistics in an approximate quantum dynamics method. We start by noting that it is easy to show that the Kubo-transformed quantum thermal correlation function (TCF) has a classical analog at $t = 0$,

$$\tilde{c}_{AB}(0) \approx \lim_{P\to\infty} \int d\{\mathbf{p}_\alpha\} \int d\{\mathbf{R}_\alpha\} e^{-\beta_P H_P(\mathbf{R}_\alpha, \mathbf{p}_\alpha)} A_P(\mathbf{R}_0) B_P(\mathbf{R}_0) \tag{2.32}$$

where, again, the functions $A_P(\mathbf{R}_0)$ and $B_P(\mathbf{R}_0)$ are averaged over the beads of the ring polymer at $t = 0$,

$$A_P(\mathbf{R}) = \frac{1}{P}\sum_{\alpha=1}^{P} A(\mathbf{R}_\alpha), \quad B_P(\mathbf{R}) = \frac{1}{P}\sum_{\alpha=1}^{P} B(\mathbf{R}_\alpha) \tag{2.33}$$

and H_P refers to the classical ring polymer Hamiltonian in Eq. (2.19). By taking the fictitious mass, M, in the momenta term in Eq. (2.19), to be the physical mass of the system, we can generate an ensemble average of classical trajectories. This ensemble average of trajectories provides a classical-like approximation to the Kubo-transformed quantum correlation function. RPMD approximates Eq. (2.29) for $t > 0$ such that,

$$\tilde{c}_{AB}(t) \approx \lim_{P\to\infty} \int d\{\mathbf{p}_\alpha\} \int d\{\mathbf{R}_\alpha\} e^{-\beta_P H_P(\mathbf{R}_\alpha, \mathbf{p}_\alpha)} A_P(\mathbf{R}_0) B_P(\mathbf{R}_t) \tag{2.34}$$

The evaluation of Eq. (2.34) involves initializing a distribution of ring polymer extended phase space configurations using PIMC or PIMD. Subsequently, an ensemble of ring polymer MD trajectories are launched from this distribution

and propagated under the ring polymer Hamiltonian, H_P, with dynamic properties averaged over the ensemble.

Features of RPMD

The RPMD approximation of the correlation function, $\tilde{c}_{AB}(t)$, is a classical correlation function in the extended ring polymer phase space of the P-bead imaginary time path integral. In the limit of high temperature, the harmonic spring force constant, MP^2/β^2, becomes so large that the radius of gyration of the ring polymer shrinks to zero, which corresponds to a single-bead limit.

It can be shown that RMPD correlation functions give the exact Kubo-transformed quantum mechanical correlation function as $t \to 0$ by expanding both in a Taylor series about $t = 0$, considering the case where $A(\hat{R})$ and $B(\hat{R})$ are hermitian operators [38]. Even coefficients of the expansion of both terms are the only ones to survive since $\tilde{c}_{AB}(t)$ and RPMD correlations functions are real and even. Upon comparing terms in the expansion it is revealed that RPMD has a leading $O(t^8)$ error term for position autocorrelation functions and $O(t^4)$ for general correlation functions with nonlinear operators [**?**].

If the system potential, $V(\hat{R})$, is harmonic, Eq. 2.19 will give the exact quantum result in the limit as $P \to \infty$ for all correlation functions of the form $\tilde{c}_{Aq}(t)$ and $\tilde{c}_{qB}(t)$. For the case of position autocorrelation functions, $\tilde{c}_{qq}(t)$, RPMD gives the exact result for any value of P [39].

Justification and Applicability

While Hele and co-workers published a derivation establishing the connection between the RPMD approximation made in Eq. (2.34) and the Kubo-transformed correlation function in Eq. (2.29) [40, 41], a detailed understanding of the physical nature of the approximation has yet to be reported. Despite the lack of a rigorous proof for the RPMD approximation for $t > 0$, the use of RPMD has been justified on numerous grounds.

First, as mentioned previously, the connection between RPMD transition state theory and quantum transition state theory ($t \rightarrow 0^{+}$) has been reported in the literature [40, 41]. Further, the mathematical relationship between RPMD as approximate dynamics and exact quantum Matsubara dynamics brings us closer to a complete proof of the RPMD approximation [42, 43]. Moreover, Richardson and co-workers showed that RPMD rate theory in the deep tunneling regime is connected to semiclassical instanton theory, namely the "ImF" method [3]. It is also worth noting that our knowledge of RPMD's quantum approximations widely inform our choice of application. We can first see this by considering the harmonic spring terms in the ring polymer Hamiltonian which, unlike a single classical particle, incorporate ZPE, and accurately describes the delocalized nature of a quantum particle. The latter feature represents the quantum dispersion as well as quantum mechanical tunneling through an energy barrier.

A significant shortcoming of the RPMD approximation is in its central assumption that real-time quantum coherences dissipate rapidly in condensed phase chemical systems. The method's inability to accurately account for quantum coherence effects result in its failure to capture quantum features such as

Rabi oscillations [38]. Specifically, this is due to the lack of phase information in the RPMD equations of motion. Consequently, RPMD is most useful in condensed phase systems where thermal averaging and strong inter-mode coupling are dominant resulting in rapid quantum decoherence. Despite these shortcomings RPMD has proven to be quite accurate in the study of single particle processes such as proton transfer (PT) and electron transfer (ET) [44, 45].

If we wish to use RPMD to study dynamic processes involving the motion of multiple quantum particles, we must address RPMD's single surface and single particle limitations. The issue of RPMD being a single surface method restricts its use to adiabatic processes where electrons and nuclei move on widely differing time scales. This has influenced multiple efforts toward nonadiabatic extensions of RPMD such as surface hopping RPMD [21], KC-RPMD [46, 22], Coherent-state RPMD [23], MV-RPMD (which is the focus of this study) [2, 27, 28], nonadiabatic MF-RPMD [24] and more [26]. In regards to the latter issue, the method's treatment of quantum particles as unique renders it an inviable method for studying the dynamics of indistinguishable quantum particles such as fermions and bosons. In order for the second issue to be corrected, the distribution that falls out of the path integral discretization of the QBD would have to accurately account for fermionic or bosonic statistics. While there have been numerous studies on the fermionic and bosonic extension of PIMD and PIMC for capturing fermionic statistics [47, 48], there are limited dynamic studies of identical particles in the condensed phase.

Next we will discuss some past developments of nondiabatic RPMD theories and their limitations. Subsequently we will discuss the MV-RPMD formalism in detail, all of which will motivate our efforts toward applying RPMD to in-

teresting nonadiabatic systems such as photochemical processes. The challenge remains in how we describe the discrete system states. We will show how to represent discrete system states with continuous coordinates that can be integrated in a classical MD simulation within the RPMD framework.

2.2 Review of MV-RPMD Formalism

2.2.1 Nonadiabaticity in RPMD

One of the first efforts to extend RPMD for treatment of nonadiabatic systems was the development of KC-RPMD [22, 46]. The KC-RPMD method employs a continuous collective variable which reports on kink-pair formation. The collective variable used in tandem with a constraint on kink-pairs has proven to be highly accurate for rate calculations of ET in a wide range of regimes [22, 46]. While KC-RPMD is highly accurate across a wide range of regimes, it does not preserve the QBD and is limited to two-state systems [22, 46]. Nonadiabatic RPMD, developed by Jeremy Richardson and co-workers [26] resolves the two-state limitation of KC-RPMD by treating discrete states with continuous harmonic oscillator variables. Despite this improvement, nonadiabatic RPMD also fails to preserve the QBD.

Nonadiabatic MF-RPMD, which was recently developed by a former member of our group Jessica Duke [24], was shown to be accurate in the calculation of ET rates across all regimes. This method is general for multi-electron systems, multiple states and preserves the QBD. While nonadiabatic MF-RPMD is successful at capturing ET rates across all regimes, it is limited to systems starting

in thermal equilibrium. Ideally we would like a nonadiabatic version of RPMD that is amenable to excited state (non-equilibrium) dynamics and would allow for the study of photochemical processes such as singlet fission and photosynthesis. Moving toward this goal, our group has used MV-RPMD in the past to simulate photo-initiated dynamics in the gas phase [27]. The novel work presented in this dissertation is the first application of MV-RPMD in the condensed phase toward proton coupled electron transfer (PCET) reactions. Before we get into applications of MV-RPMD, we will review the MV-RPMD formalism.

2.2.2 Mapping Variable Ring Polymer Molecular Dynamics

The Hamiltonian for a general K-level system is

$$\hat{H} = \frac{\mathbf{P}^T\mathbf{P}}{2M} + V_0(\mathbf{R}) + \sum_{n,m=1}^{K} |\psi_n\rangle V_{nm}(\mathbf{R})\langle\psi_m|, \tag{2.35}$$

where $\mathbf{R}, \mathbf{P}$ are nuclear position and momentum operators respectively, $V_0(\mathbf{R})$ is a state independent nuclear potential, $V_{nm}(\mathbf{R})$ are elements of the diabatic potential energy matrix, and $|\psi_n\rangle$ represents the n^{th} electronic state. Implementing the Meyer-Miller-Stock-Thoss protocol [49], we map the electronic states to singly excited oscillator (SEO) states,

$$|\psi_n\rangle\langle\psi_m| \rightarrow a_n^\dagger a_m \equiv |n\rangle\langle m|, \tag{2.36}$$

where $a_n^\dagger$ and a_m are boson creation and annihilation operators respectively that obey the commutation rules $[a_n^\dagger, a_m] = \delta_{nm}$. In Eq. (2.36), we use the notation $|n\rangle = |0_1 0_2 \ldots 1_n \ldots 0_K\rangle$, to represent SEO states that correspond to a product of $K-1$ uncoupled oscillators in the ground state and one oscillator in the first excited state. Following the original MV-RPMD derivation, path integral discretization

of the canonical partition function, $Z = \mathrm{Tr}\left[e^{-\beta\hat{H}}\right]$ where $\beta = 1/kT$, is performed using continuous Cartesian variables for the electronic and nuclear degrees of freedom by inserting $N-1$ copies of the identity,

$$I = \int d\mathbf{x} \int d\mathbf{R}\ |\mathbf{x},\mathbf{R}\rangle\langle\mathbf{x},\mathbf{R}|\mathcal{P}, \tag{2.37}$$

where $\mathcal{P} \equiv \sum_n |n\rangle\langle n|$ is the projection operator in the SEO basis. Evaluating the matrix elements of the Boltzmann operator using the symmetric Trotter approximation (see Section 2.3) and employing a Wigner transform in the electronic variables, we obtain an exact path integral expression for the quantum Boltzmann distribution in electronic and nuclear phase space variables,

$$\begin{aligned} Z \ \propto\ & \lim_{N\to\infty} \int d\{\mathbf{R}_\alpha\} \int \mathbf{d}\{\mathbf{P}_\alpha\} \int \mathbf{d}\{\mathbf{x}_\alpha\} \int \mathbf{d}\{\mathbf{p}_\alpha\} \\ & \times e^{-\beta_N H_N(\{\mathbf{R}_\alpha\},\{\mathbf{P}_\alpha\},\{\mathbf{x}_\alpha\},\{\mathbf{p}_\alpha\})} \mathrm{sgn}(\Theta), \end{aligned} \tag{2.38}$$

where $\beta_N = \beta/N$, $\int d\{\mathbf{R}_\alpha\} \equiv \int d\mathbf{R}_1 \int d\mathbf{R}_2 \ldots \int d\mathbf{R}_N$ and similarly for the other variables of integration. In Eq. (2.38), the MV-RPMD Hamiltonian is

$$H_N = H_{RP} + \sum_{\alpha=1}^{N} \left(\frac{1}{\beta_N} \mathbf{x}_\alpha^T \mathbf{x}_\alpha + \frac{1}{\beta_N} \mathbf{p}_\alpha^T \mathbf{p}_\alpha \right) - \frac{1}{\beta_N} \ln|\Theta|, \tag{2.39}$$

where N is the number of ring polymer beads, and the nuclear ring polymer Hamiltonian,

$$\begin{aligned} H_{RP} \ =\ & \sum_{\alpha=1}^{N} \Big[\frac{\mathbf{P}_\alpha^T \cdot \mathbf{P}_\alpha}{2M} + V_0(\mathbf{R}_\alpha) \\ & + \frac{1}{2} M \omega_N^2 (\mathbf{R}_\alpha - \mathbf{R}_{\alpha+1})^T \cdot (\mathbf{R}_\alpha - \mathbf{R}_{\alpha+1}) \Big], \end{aligned} \tag{2.40}$$

where M is the physical mass of the nuclei, and $\omega_N = N/\beta$. The electron-nuclear interaction term in Eq. (2.39) is

$$\Theta = \mathrm{Re}(\mathrm{Tr}[\mathbf{\Gamma}]), \tag{2.41}$$

where

$$\mathbf{\Gamma} = \prod_{\alpha=1}^{N} (C_\alpha - \frac{1}{2}\mathcal{I}) \mathcal{M}(\mathbf{R}_\alpha, \mathbf{R}_{\alpha+1}), \tag{2.42}$$

$$C_\alpha = (\mathbf{x}_\alpha + i\mathbf{p}_\alpha) \otimes (\mathbf{x}_\alpha - i\mathbf{p}_\alpha)^T, \tag{2.43}$$

and $\mathbf{x}_\alpha$, $\mathbf{p}_\alpha$ are continuous position and momentum vectors of length K representing the K electronic states of the α^{th} ring polymer bead. Finally, the interaction matrix in Eq. (2.42) is given by

$$\mathcal{M}_{nm}(\mathbf{R}_\alpha, \mathbf{R}_{\alpha+1}) = \begin{cases} e^{-\frac{\beta_N}{2}[V_{nn}(\mathbf{R}_\alpha)+V_{nn}(\mathbf{R}_{\alpha+1})]} + \mathcal{O}(\beta_N^2) & n = m \\ \sum_{j\neq n} -\frac{\beta_N}{4}[V_{nj}(\mathbf{R}_\alpha) + V_{nj}(\mathbf{R}_{\alpha+1})]e^{-\frac{\beta_N}{2}[V_{jj}(\mathbf{R}_\alpha)+V_{jj}(\mathbf{R}_{\alpha+1})]} & n \neq m \\ \quad + \sum_{j\neq m} -\frac{\beta_N}{4}[V_{jm}(\mathbf{R}_\alpha) + V_{jm}(\mathbf{R}_{\alpha+1})]e^{-\frac{\beta_N}{2}[V_{jj}(\mathbf{R}_\alpha)+V_{jj}(\mathbf{R}_{\alpha+1})]} + \mathcal{O}(\beta_N^2) & \end{cases}, \tag{2.44}$$

a result that is well known in the context of state space path integrals. The interaction matrix in Eq. (2.44) is symmetric (in keeping with the original quantum Hamiltonian) making the MV-RPMD Hamiltonian symmetric, and improving the numerical stability of the approximate dynamics. We also emphasize that the symmetric and asymmetric formulations are equivalent for equilibrium simulations and exhibit similar bead-convergence properties.

2.3 Symmetrized Trotter Approximation

In the limit that $N \to \infty$, the high-temperature symmetric Trotter approximation is used to separate the state independent nuclear potential operator, V_0 and the diabatic potential energy matrix, V, from the nuclear kinetic operator T,

$$\begin{aligned} &\langle n, R_\alpha | e^{-\beta_N H} | R_{\alpha+1}, m\rangle \\ &\approx \langle n, R_\alpha | e^{-\frac{\beta_N}{2}V_0} e^{-\frac{\beta_N}{2}V} e^{-\beta_N T} e^{-\frac{\beta_N}{2}V} e^{-\frac{\beta_N}{2}V_0} | R_{\alpha+1}, m\rangle \\ &= e^{-\frac{\beta_N}{2}(V_0(R_\alpha)+V_0(R_{\alpha+1}))} \langle R_\alpha | e^{-\beta_N T} | R_{\alpha+1}\rangle \\ &\quad \times \langle n | e^{-\frac{\beta_N}{2}V(R_\alpha)} e^{-\frac{\beta_N}{2}V(R_{\alpha+1})} | m\rangle. \end{aligned} \tag{2.44}$$

The nuclear kinetic matrix element can be evaluated exactly to obtain

$$\langle R_\alpha | e^{-\beta_N T} | R_{\alpha+1}\rangle$$

$$
\begin{aligned}
&= \int dP \langle R_\alpha | P \rangle \langle P | e^{-\beta_N T} | R_{\alpha+1} \rangle \\
&= \int dP \langle R_\alpha | P \rangle e^{-\beta_N P^2/2m} \langle P | R_{\alpha+1} \rangle \\
&= \left(\frac{M}{2\pi\beta_N} \right)^{1/2} e^{-\frac{\beta_N}{2} M \omega_N^2 (R_\alpha - R_{\alpha+1})^2}.
\end{aligned} \tag{2.45}
$$

Substituting Eq. (2.46) back in the Boltzmann matrix element, we have

$$
\begin{aligned}
&\langle n, R_\alpha | e^{-\beta_N H_N} | R_{\alpha+1}, m \rangle \\
&\approx \left(\frac{M}{2\pi\beta_N} \right)^{1/2} e^{-\frac{\beta_N}{2} \left(V_0(R_\alpha + V_0(R_{\alpha+1}) + \frac{M\omega_N^2}{2} (R_\alpha - R_{\alpha+1})^2 \right)} \\
&\quad \times \langle n | e^{-\frac{\beta_N}{2} [V(R_\alpha) + V(R_{\alpha+1})]} | m \rangle.
\end{aligned} \tag{2.46}
$$

In order to evaluate the electronic matrix element, we begin by defining a diagonal matrix with elements, $V_{\mathrm{D}}(R_\alpha, R_{\alpha+1}) = \frac{1}{2}(V_{\mathrm{D}}(R_\alpha) + V_{\mathrm{D}}(R_{\alpha+1}))$, and off-diagonal matrix elements $V_{\mathrm{OD}}(R_\alpha, R_{\alpha+1}) = \frac{1}{2}(V_{\mathrm{OD}}(R_\alpha) + V_{\mathrm{OD}}(R_{\alpha+1}))$. Employing a high-temperature Trotter approximation, we further split the off-diagonal terms symmetrically around the diagonal terms to obtain

$$
\begin{aligned}
&\langle n | e^{-\beta_N (V_{\mathrm{D}} + V_{\mathrm{OD}})} | m \rangle \\
&\approx \langle n | e^{\frac{-\beta_N}{2} V_{\mathrm{OD}}} e^{-\beta_N V_{\mathrm{D}}} e^{\frac{-\beta_N}{2} V_{\mathrm{OD}}} | m \rangle \\
&= \sum_{j,k} \langle n | e^{\frac{-\beta_N}{2} V_{\mathrm{OD}}} | j \rangle \langle j | e^{-\beta_N V_{\mathrm{d}}} | k \rangle \langle k | e^{\frac{-\beta_N}{2} V_{\mathrm{OD}}} | m \rangle \\
&= \sum_{j} \langle n | e^{\frac{-\beta_N}{2} V_{\mathrm{OD}}} | j \rangle e^{-\beta_N V_{jj}} \langle j | e^{\frac{-\beta_N}{2} V_{\mathrm{OD}}} | m \rangle.
\end{aligned} \tag{2.47}
$$

The off-diagonal matrix elements are easily evaluated,

$$
\begin{aligned}
\langle n | e^{\frac{-\beta_N}{2} V_{\mathrm{OD}}} | j \rangle &\approx \langle n | (1 - \frac{\beta_N}{2} V_{\mathrm{OD}}) | j \rangle + O(\beta_N^2) \\
&= \begin{cases} 1 & n = j \\ \frac{\beta_N}{2} [V_{\mathrm{OD}}]_{n,j} & n \neq j \end{cases}
\end{aligned} \tag{2.48}
$$

where $[V]_{nm}$ is used to indicate off-diagonal elements of the diabatic potential energy matrix. Substituting Eq. (2.49) into Eq.(2.48), we obtain an expression

for the electronic matrix elements by considering two cases: **Case 1 ($n = m$):** If $n = j$

$$\begin{aligned} &\langle n|e^{-\beta_N(V_D+V_{OD})}|n\rangle \\ &= \langle n|e^{\frac{-\beta_N}{2}V_{OD}}|n\rangle e^{-\beta_N V_{nn}}\langle n|e^{\frac{-\beta_N}{2}V_{OD}}|n\rangle = e^{-\beta_N V_{nn}} \end{aligned} \tag{2.49}$$

If $n \neq j$

$$\begin{aligned} &\langle n|e^{-\beta_N(V_D+V_{OD})}|n\rangle \\ &= \sum_{n\neq j}\langle n|e^{\frac{-\beta_N}{2}V_{OD}}|j\rangle e^{-\beta_N V_{jj}}\langle j|e^{\frac{-\beta_N}{2}V_{OD}}|n\rangle \\ &= \sum_{n\neq j}\left(\frac{-\beta_N}{2}\right)^2 V_{nj}^2 e^{-\beta_N V_{jj}} = 0 + O(\beta_N^2) \end{aligned} \tag{2.50}$$

Case 2 ($n \neq m$): If $n = j$ and if $m \neq j$

$$\begin{aligned} &\sum_{m\neq j}\langle n|e^{\frac{-\beta_N}{2}V_{OD}}|j\rangle e^{-\beta_N V_{jj}}\langle j|e^{\frac{-\beta_N}{2}V_{OD}}|m\rangle \\ &= \sum_{m\neq j} -\frac{\beta_N}{2}V_{jm}e^{-\beta_N V_{jj}} \end{aligned} \tag{2.51}$$

If $n \neq j$ and if $m = j$

$$\begin{aligned} &\sum_{n\neq j}\langle n|e^{\frac{-\beta_N}{2}V_{OD}}|j\rangle e^{-\beta_N V_{jj}}\langle j|e^{\frac{-\beta_N}{2}V_{OD}}|m\rangle \\ &= \sum_{n\neq j} -\frac{\beta_N}{2}V_{nj}e^{-\beta_N V_{jj}} \end{aligned} \tag{2.52}$$

If $n \neq j$ and if $m \neq j$

$$\begin{aligned} &\sum_{n\neq m\neq j}\langle n|e^{\frac{-\beta_N}{2}V_{OD}}|j\rangle e^{-\beta_N V_{jj}}\langle j|e^{\frac{-\beta_N}{2}V_{OD}}|m\rangle \\ &= \sum_{n\neq m\neq j}\left(\frac{\beta_N}{2}\right)^2 V_{nj}V_{jm}e^{-\beta_N V_{jj}} = 0 + O(\beta_N^2) \end{aligned} \tag{2.53}$$

2.3.1 Implementation Details

In order to measure the improvement in equilibrium statistics due to symmetrization of the Trotter splitting we consider equilibrium properties of a model ET system. These include state-specific nuclear probability distributions, and the average total energy. All equilibrium simulations were performed using standard path integral Monte Carlo (PIMC) importance sampling techniques, although the use of PIMD is also straight forward. The nuclear probability distribution is defined as,

$$P(n,\mathbf{R}) = \frac{\mathrm{tr}[\delta(\mathbf{R}-\hat{\mathbf{R}})|n\rangle\langle n|e^{-\beta\hat{H}}]}{\mathrm{tr}[e^{-\beta\hat{H}}]} \tag{2.54}$$

which can be written as,

$$\frac{\langle\delta(\mathbf{R}-\mathbf{R_P})\frac{\Gamma_{nn}}{\mathrm{tr}[\Gamma]}\mathrm{sgn}(\Theta)\rangle_W}{\langle\mathrm{sgn}(\Theta)\rangle_W} \tag{2.55}$$

where the angular brackets indicate average is taken with respect to sampling function, $W = e^{-\beta_N H_N(\{\xi_\alpha\}_\mathbf{0})}$, and $\{\xi_\alpha\}_\mathbf{t}$ represents the set of bead positions and momenta $\{\mathbf{R}_\alpha, \mathbf{P}_\alpha, \mathbf{x}_\alpha, \mathbf{p}_\alpha\}$, and Γ is,

$$\mathbf{\Gamma} = \prod_{\alpha=1}^{N}(C_\alpha - \frac{1}{2}\mathcal{I})\mathcal{M}(\mathbf{R}_\alpha, \mathbf{R}_{\alpha+\mathbf{1}}), \tag{2.56}$$

$$C_\alpha = (\mathbf{x}_\alpha + i\mathbf{p}_\alpha)\otimes(\mathbf{x}_\alpha - i\mathbf{p}_\alpha)^T. \tag{2.57}$$

Γ_{nn} is Γ projected on to a particular electronic state n. The average total energy of the system is obtained using a primitive energy estimator,

$$\langle E\rangle = -\frac{1}{Z}\frac{\partial Z}{\partial\beta}. \tag{2.58}$$

where,

$$-\frac{1}{Z}\frac{\partial Z}{\partial\beta} = \sum_\alpha^P \frac{P_\alpha^2}{2MP} + \frac{mP}{2\beta^2}\sum_{\alpha=1}^{P}(R_\alpha - R_{\alpha+1})^2 + \frac{1}{P}\sum_{\alpha=1}^{P}V(R_\alpha) - \frac{1}{\Theta}\frac{\partial\Theta}{\partial\beta}. \tag{2.59}$$

2.3.2 Equilibrium Simulation Result: Model ET

We test the statistical improvements due to the symmetrized QBD by studying the equilibrium properties of a model ET system developed by Ananth and Miller [44]. The diabatic matrix elements are defined by,

$$V_{11} = a_1 s^2 + b_1 s + c_1 \tag{2.60}$$

and,

$$V_{22} = a_2 s^2 + b_2 s + c_2. \tag{2.61}$$

The parameters for the diagonal elements are reported in Table 2.1. and the

Diabat	a	b	c
V_{11}	4.7722×10^{-3}	1.1308×10^{-2}	-2.1576
V_{22}	4.7722×10^{-3}	-1.1308×10^{-2}	-2.1576

Table 2.1: Diabatic potential energy surface parameters for ET model

constant off-diagonal coupling is $V_{12} = V_{21} = 2.0662 \times 10^{-5}$. We run simulations

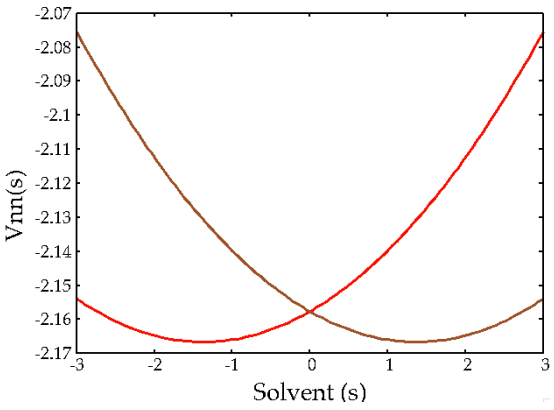

Figure 2.1: Diabatic potential energy curves for ET model with state 1 in red and state 2 in brown

at 300 K ($\beta = 1052$a.u.). Fig (2.2) shows the average energy bead convergence

for the model ET system using the symmetrized QBD. Convergence is achieved with 5 beads to give an average energy of 5.36×10^{-3} with error bars on the order of 10^{-6}. We compared these results to bead convergence achieved with the asymmetric QBD and found that at 6 beads, the symmetrized QBD generates statistics with error bars an order of magnitude smaller than the asymmetric QBD. This suggests that the symmetrized Trotter splitting of the diabatic matrix increases the stability of the statistics. This is attributed to the fact that the elements in the symmetrized diabatic matrix are symmetrically modulated by neighboring beads.

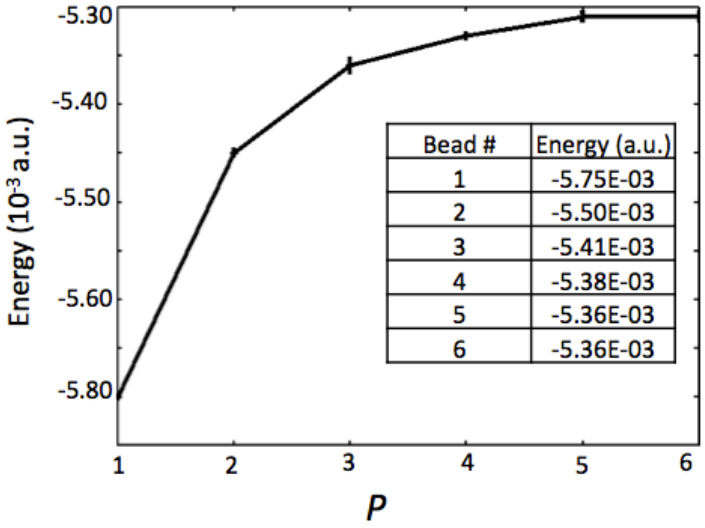

Figure 2.2: Average energy bead convergence

2.3.3 MV-RPMD Trajectories and Correlation Functions

In general, thermal real-time correlation functions in the MV-RPMD framework are written as

$$C_{AB}(t) = \frac{\langle \mathrm{sgn}(\Theta) A(\{\xi_\alpha\}_\mathbf{0}) \mathbf{B}(\{\xi_\alpha\}_\mathbf{t}) \rangle_\mathbf{W}}{\langle \mathrm{sgn}(\Theta) \rangle_W}, \tag{2.62}$$

where $\{\xi_\alpha\}_\mathbf{t}$ represents the set of bead positions and momenta $\{\mathbf{R}_\alpha, \mathbf{P}_\alpha, \mathbf{x}_\alpha, \mathbf{p}_\alpha\}$ at time t, and the bead-averaged function $A(\{\xi_\alpha\}_0) = 1/N \sum_\alpha A(\xi_\alpha(\mathbf{0}))$ and $B(\{\xi_\alpha\}_\mathbf{t})$ is similarly defined. The initial positions and momenta are generated from a standard Path Integral Monte Carlo (PIMC) simulation that employs the sampling function, W. This corresponds to a system initially at equilibrium, $W = e^{-\beta_N H_N(\{\xi_\alpha\}_\mathbf{0})}$, with the MV-RPMD Hamiltonian, H_N, defined in Eq. (2.39). However, this function can also be defined to describe an initial non-equilibrium distribution as discussed later on (see Section 4.4). Real-time trajectories are generated by integrating equations of motion corresponding to the MV-RPMD Hamiltonian,

$$\begin{aligned} \dot{\mathbf{R}}_\alpha &= \frac{\partial H_P}{\partial \mathbf{P}_\alpha}, \; \dot{\mathbf{P}}_\alpha = -\frac{\partial H_P}{\partial \mathbf{R}_\alpha} \\ \dot{\mathbf{x}}_\alpha &= \frac{\partial H_P}{\partial \mathbf{p}_\alpha}, \; \dot{\mathbf{p}}_\alpha = -\frac{\partial H_P}{\partial \mathbf{x}_\alpha}. \end{aligned} \tag{2.63}$$

These trajectories preserve the QBD for a P-level system. Upon evaluating the derivatives in terms of H_P in Eq. (2.39) we get,

$$\dot{\mathbf{R}}_\alpha = \frac{\mathbf{P}_\alpha}{M} \tag{2.64}$$

$$\dot{\mathbf{P}}_\alpha = -\frac{MP}{\beta^2}(2\mathbf{R}_\alpha - \mathbf{R}_{\alpha+1} - \mathbf{R}_{\alpha-1}) - \left(\frac{\partial V_0}{\partial \mathbf{R}_\alpha}\right) - \frac{P}{\beta\Theta}\left(\frac{\partial \Theta}{\partial \mathbf{R}_\alpha}\right) \tag{2.65}$$

$$[\dot{\mathbf{x}}_\alpha]_j = \frac{2P}{\beta}[\mathbf{p}_\alpha]_j - \frac{P}{\beta\Theta}\left(\frac{\partial \Theta}{\partial [\mathbf{p}_\alpha]_j}\right) \tag{2.66}$$

$$[\dot{\mathbf{p}}_\alpha]_j = -\frac{2P}{\beta}[\mathbf{x}_\alpha]_j + \frac{P}{\beta\Theta}\left(\frac{\partial \Theta}{\partial [\mathbf{x}_\alpha]_j}\right) \tag{2.67}$$

where $[]_j$ refers to the j^{th} component of the electronic variable. Again, real-time TCFs in the RPMD framework are identical to the Kubo-transformed correlation functions at time zero and the same is true for MV-RPMD TCFs. For example the Kubo-transformed nuclear position-position TCF is,

$$\tilde{c}_{RR}(t) = \frac{1}{\beta Z}\int_0^\beta \mathrm{tr}[e^{-(\beta-\lambda)\hat{H}}\hat{R}(0)e^{-\lambda\hat{H}}\hat{R}(t)]d\lambda \tag{2.68}$$

and the corresponding MV-RPMD correlation function is written as,

$$C_{RR}^{\mathrm{MVR}}(t) = \frac{1}{Z}\int d\{\mathbf{x}_\alpha\}\int d\{\mathbf{p}_\alpha\}\int d\{\mathbf{R}_\alpha\}\int d\{\mathbf{P}_\alpha\}e^{-\beta_P H_P(\{\mathbf{x}_\alpha\},\{\mathbf{x}_\alpha\},\{\mathbf{x}_\alpha\},\{\mathbf{x}_\alpha\})}\bar{\mathbf{R}}(0)\bar{\mathbf{R}}(t)\mathrm{sgn}(\Theta). \tag{2.69}$$

where

$$\bar{\mathbf{R}} = \frac{1}{P}\sum_{\alpha=1}^{P}\mathbf{R}_\alpha. \tag{2.70}$$

2.4 Summary

In this chapter we reviewed the imaginary-time path integral discretization of the QBD which results in what is known to be the classical isomorphism between the classical statistics of a ring polymer and the exact quantum statistics of a quantum particle. We explored the basic theory of RPMD, an efficient yet approximate method that preserves the QBD and provides a consistent dynamic framework for reaction dynamics. We mentioned some of the limitations of RPMD, including its inability to capture real-time quantum coherence beyond $t = \beta\hbar$, and describe multi-electron/multi-state quantum systems. We described nonadiabtatic extensions of RPMD, including MV-RPMD and nonadiabatic MF-RPMD (both developed in our group) and their applications to classes of nonadiabatic reactions.

We then provided a derivation of an improved QBD in the MV-RPMD framework where the symmetric Trotter approximation is invoked and generated statistics for a model ET system with increased stability in convergence. We also provided the mathematical formalism required to generate approximate quantum dynamics in the MV-RPMD framework with the goal of calculating real-time TCFs.

Given MV-RPMD's success at capturing excited state dynamics in the gas phase, it is now of interest to consider nonadiabatic multi-particle reactions in the condensed phase. Eventually we'd like to use MV-RPMD in the simulation of proton coupled electron transfer reactions. The next section will review some of the PCET model systems reported in the literature which will set the ground work for PCET simulations in the condensed phase with MV-RPMD.

CHAPTER 3

MODELING PCET

PCET reactions are typically described in terms of a reactant, metastable intermediate, and product species,

$$D - H + A \quad (D_eD_p) \tag{3.1}$$

$$[D - H]^+ + A^- \quad (A_eD_p) \tag{3.2}$$

$$D^- + [H - A]^+ \quad (D_eA_p) \tag{3.3}$$

$$D + H - A \quad (A_pA_e) \tag{3.4}$$

Here D and A represent donor and acceptor molecules respectively, and D_eD_p corresponds to both the electron and proton being on the donor, D_eA_p correspond to the electron being on the donor and the proton being on the acceptor, D_pA_e corresponds to the electron being on the acceptor and the proton being on the donor, and A_pA_e corresponds to both the electron and the proton being on the acceptor. The reaction mechanism can be categorized as either sequential or concerted depending whether both the electron and proton transfer in a single step. In the concerted mechanism the proton and electron transfer simultaneously without the formation of metastable intermediates. In the sequential mechanism you can have either the proton transfer first, forming the metastable D_eA_p species, followed by electron transfer to form the product A_pA_e species. Conversely in a sequential mechanism an electron can transfer first, forming the intermediate species A_eD_p, followed by proton transfer to form the product species A_pA_e.

3.1 Model Systems

In this section we will review the various PCET model systems that have been reported in the literature as well as the model PCET system we develop in this study. Further, we will comment on the extent of RPMD and MV-RPMD's applicability across model systems.

3.1.1 Capped Coulomb Potentials Coupled to Proton Double Well

The first model to consider for PCET is a colinear system bath model [50], where in the position representation we have the potential energy function,

$$U(q_e, q_p, q_s, \mathbf{Q}) = U_{sys}(q_e, q_p, q_s) + U_B(q_s, \mathbf{Q}) \tag{3.5}$$

where $U_B(q_s, \mathbf{Q})$ is the potential energy term associated with the bath coordinate, and system potential energy is,

$$U_{sys}(q_e, q_p, q_s) = U_e(q_e) + U_p(q_p) + U_s(q_s) + U_{es}(q_e, q_s) + U_{ps}(q_p, q_s) + U_{ep}(q_p, q_e) \tag{3.6}$$

The variables q_e, q_p, q_s, are scalar coordinates that describe the positions of the electron, electron, proton and solvent respectively. The vector $\mathbf{Q}$ describes the bath oscillator positions. The first term in the system potential models the interaction between the transferring electron and the donor and acceptor sites,

$$U_e(q_e) = \begin{cases} a_D q_e^2 + b_D q_e + c_D, & r_D^{\text{out}} \leq q_e \leq r_D^{\text{in}} \\ a_A q_e^2 + b_A q_e + c_A, & r_A^{\text{out}} \leq q_e \leq r_A^{\text{in}} \\ -\mu_e \left[\frac{1}{q_e - r_d} + \frac{1}{q_e - r_d} \right], & \text{otherwise} \end{cases} \tag{3.7}$$

In Eq. (3.7) r_D and r_A are the positions of the electron donor and acceptor sites. This model consists of two symmetric Coulombic wells which are capped by quadratic functions to remove singularities. The second term, $U_p(q_p)$, is a quartic potential which models the interaction between the transferring proton and the donor and acceptor cites,

$$U_p(q_p) = -\frac{m_p\omega_p^2}{2}q_p^2 + \frac{m_p^2\omega_p^4}{16V_0}q_p^4. \tag{3.8}$$

Here, ω_p is the proton vibrational frequency, and V_0 is the proton transfer barrier height. The solvent potential is defined as

$$U_s(q_s) = \frac{1}{2}m_s\omega_s^2q_s^2 \tag{3.9}$$

where m_s is the solvent mass, and ω_s is the effective frequency of the solvent coordinate. The coupling between the electron and solvent is defined as

$$U_{es}(q_e, q_s) = -\mu_{es}q_eq_s. \tag{3.10}$$

Similar the coupling between the electron and proton is defined as,

$$U_{ps}(q_p, q_s) = -\mu_{ep}q_pq_s. \tag{3.11}$$

Interaction between the transferring electron and proton are modeled via the capped Coulombic potential

$$U_{ep}(q_{ep}) = \begin{cases} -\frac{\mu_{ep}}{q_e-q_p}, & |q_e - q_p| > R_{cut} \\ -\frac{\mu_e}{R_{cut}}, & \text{otherwise.} \end{cases} \tag{3.12}$$

The term $U_B(q_s, \mathbf{Q})$ models the dissipative bath that is coupled to the PCET reaction. The bath exhibits an ohmic spectral density $J(\omega)$ with the cutoff frequency designated by ω_c. The density is defined as,

$$J(\omega) = \eta\omega e^{-\omega/\omega_c}, \tag{3.13}$$

where η is the friction coefficient. The density is discretized into f oscillators with frequencies defined as,

$$\omega_j = -\omega_c \ln\left(\frac{j - 0.5}{f}\right) \tag{3.14}$$

and the coupling constants are defined as

$$c_j = \omega_j \left(\frac{2\eta M \omega_c}{f\pi}\right)^{1/2}. \tag{3.15}$$

Miller and coworkers find dynamic and equilibrium calculations to converge with $P = 32$ for the proton coordinate and $P = 1024$ for the electron coordinate [51]. These bead convergence parameters depend on the mass of the quantized particle, where lighter particles require a larger number of beads. While Miller and coworkers successfully use RPMD to capture PCET rates across multiple regimes, a shortcoming is in its treatment of electron and proton as distinguishable particles. The next model PCET system discussed moves away from treating the electron as a distinguishable particle by representing discrete electron acceptor and donor states in terms of a solvent polarization coupled to a proton double well.

3.1.2 Two electronic states coupled to Proton Double Well

The next model we consider was developed by Schiffer [52] and implemented in a rate calculation using flux-side TCF by Ananth and Miller [53]. The PCET Hamiltonian is comprised of a position space proton coupled to discrete ET states defined in terms of solvent polarization. The system Hamiltonian is

$$H = \frac{P_s^2}{2m_s} + \frac{P_R^2}{2m_R} + V_p(R) + V_{ps}(R, s) + V_{ij}(R, s). \tag{3.16}$$

In Eq. (3.16), R is the proton coordinate with conjugate momentum P_R, and $V_p(R)$ is a double well potential in the proton coordinate,

$$V_p(R) = -\frac{m_R\omega_R^2}{2}R^2 + \frac{m_R^2\omega_R^4}{16V_0}R^4 - \lambda R^3, \tag{3.17}$$

where m_R is the mass of the proton, ω_R is the frequency, λ is a measure of anharmonicity, and V_0 determines the height of the barrier for proton transfer. Further, the proton-solvent coupling is

$$V_{ps}(R, s) = -\mu_1 s \tanh(\phi R), \tag{3.18}$$

where μ_1 and ϕ are constants that can be chosen to favor either concerted or sequential mechanism. The two-state diabatic potential for electron transfer is

$$V_{ii}(R, s) = \frac{1}{2}m_s\omega_s^2(s - s_i)^2 + a_i\mu_2 \tanh(\phi R), \tag{3.19}$$

where μ_2, a_i, and ϕ are constants that can be tuned to construct models that favor either concerted or sequential mechanisms. The parameter s_i is the value of the donor and acceptor potential minima for states one and two respectively. Parameters for the three models considered here are provided in Table 3.1

Parameter[a]	Model I	Model II	Model III
m_R	1836.1	1836.1	1836.1
ω_R	0.0104	0.0104	0.0104
V_0	0.012	0.014	0.012
s_1	-2.13	-2.16	-2.13
s_2	2.13	2.16	2.13
V_{12}	0.00245	0.0124	0.00245
μ_1	0.0011	0.017	-0.0011
$\mu_2 \times 10^3$	5.84	0.71	5.84
λ	0.0	0.012	0.0

Table 3.1: Parameters (in atomic units) for the model Hamiltonians in Eq. 3.16

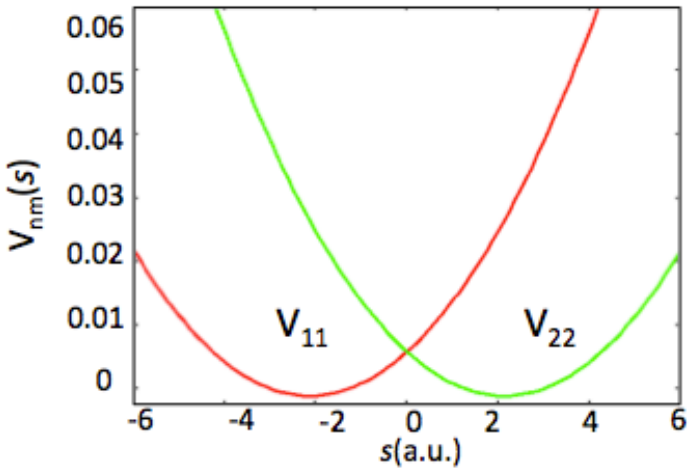

Figure 3.1: The diabatic states defined in terms of solvent polarization. $V_{11}(s)$ is shown in red and $V_{22}(s)$ is shown in green.

3.2 Concerted PCET

In Fig.(3.2) we show state-specific proton potentials, where the red curve corresponds to the proton double well coupled to the donor electronic state and the green curve corresponds to the proton double well coupled to the acceptor electronic state. The solvent/proton coupling is described by the term $V_{ps}(R, s) = -\mu_1 s \tanh(\phi R)$. We see as we move along the red curve, the stable configuration corresponds to the proton being situated at the donor. We also see, moving from left to right along the red curve, we form a metastable configuration where the electron is situated on the donor and the proton is on the acceptor. Therefore, the process of proton transfer is modeled by moving from the stable minimum on the left (proton on donor) to the metastable configuration on the right (proton on the acceptor). Subsequently, moving from the metastable configuration on the right side on the red curve to the stable con-

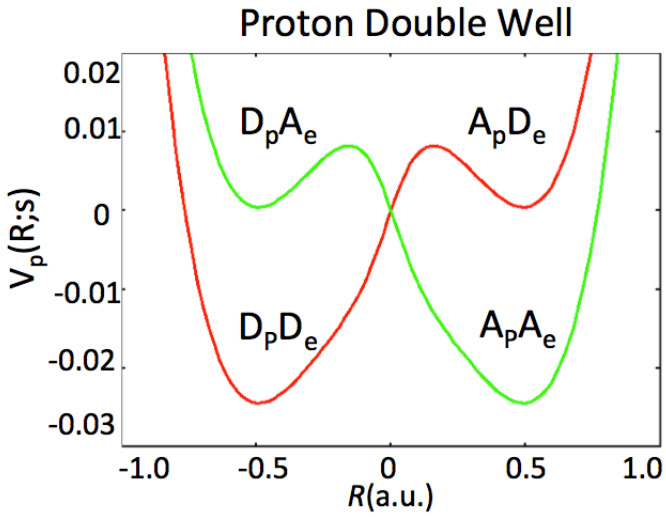

Figure 3.2: The Proton double well potential coupled to solvent polarization. $V_p(R) + V_{ps}(R; s_1)$ is shown in red and $V_p(R) + V_{ps}(R; s_2)$ is shown in green.

figuration in the right side of the green curve corresponds to ET. This process collectively would be described as sequential PT followed by ET. Moving from the stable configuration in the red curve on the left, to the metastable green curve on the left, followed by the stable configuration on the green curve on the right corresponds to sequential ET followed by PT. Finally, moving from the stable configuration in the red curve to the stable configuration on the green curve corresponds to concerted PCET.

Considering the discrete electronic states (V_{11} and V_{22}) shown in Fig. (3.1), the electron/proton coupling term $a_i\mu_2 \tanh(\phi R)$, serves to stabilize the donor electronic state when the proton is on the donor and stabilize the electronic acceptor state when the proton is on the acceptor. When the electron is on the donor and the proton is on the acceptor, $a_i\mu_2 \tanh(\phi R)$ increases the energy of V_{11} creating a metastable configuration in the electronic donor state. Similarly,

when the electron is on the acceptor and the proton is on the donor, $a_i\mu_2 \tanh(\phi R)$, increases the energy of $a_i\mu_2 \tanh(\phi R)$ creating a metastable configuration in the acceptor electronic state.

3.2.1 Equilibrium: Two State model

In our equilibrium calculations we consider the concerted PCET system (Model I). We plot average energy as a function of bead number out to $P = 16$ shown in Fig. (3.3). We run PIMC calculations out to 1×10^8 MC configurations for bead calculations less than $P = 12$ and use 1×10^9 MC configurations for higher bead calculations. We find calculations with a bead number greater than 15 for this system to be numerically demanding. Given that the proton is represented with a position-space ring polymer (RP), past studies suggest we would need at least 32 beads in the proton coordinate in order to establish convergence. We

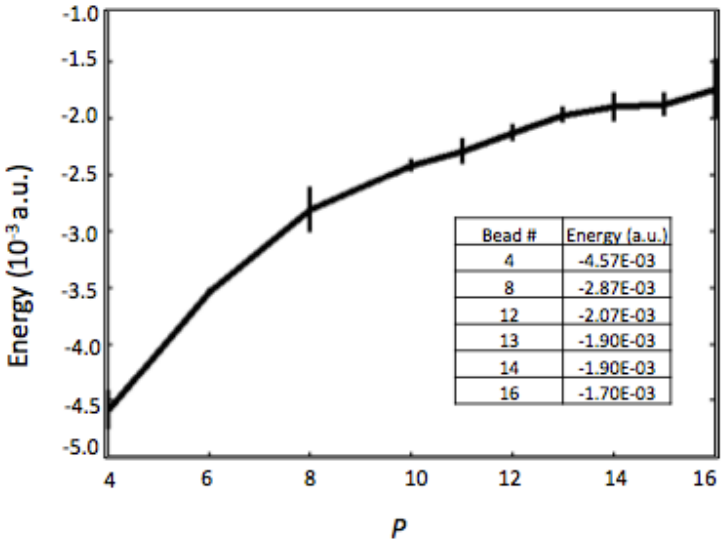

Figure 3.3: Average energy bead convergence

also calculated state-specific solvent histograms, shown in Fig. (3.4). The noise

apparent in the solvent histogram is a consequence of not establishing convergence with respect to number of MC points. Despite this, we find the peaks of the solvent histograms to be situated at the local minima of the donor and acceptor electronic states. We also calculated state-specific proton histograms,

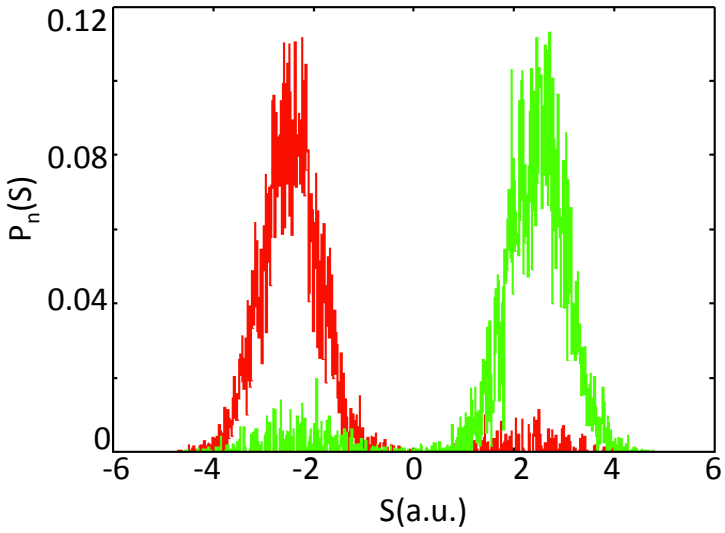

Figure 3.4: State-specific solvent histogram for concerted two state coupled to proton double well model

shown in Fig. (3.5). We find the peaks of the proton histograms to be situated at the local minima of the donor and acceptor proton configurations.

Since currently we are unable to separately quantize electronic continuous variables, and proton position space variables, the $P = 32$ requirement places unnecessary computational demands on converging calculations in the MV-RPMD representation. However, since we are working with discrete electronic states in the MV-RPMD framework (instead of a position space RP representation) convergence with respect to the electronic coordinates depend on the ratio between coupling and temperature ($\beta\Delta$). Since we are working in the weak coupling (nonadiabatic) regime for most systems we are interested in, the bur-

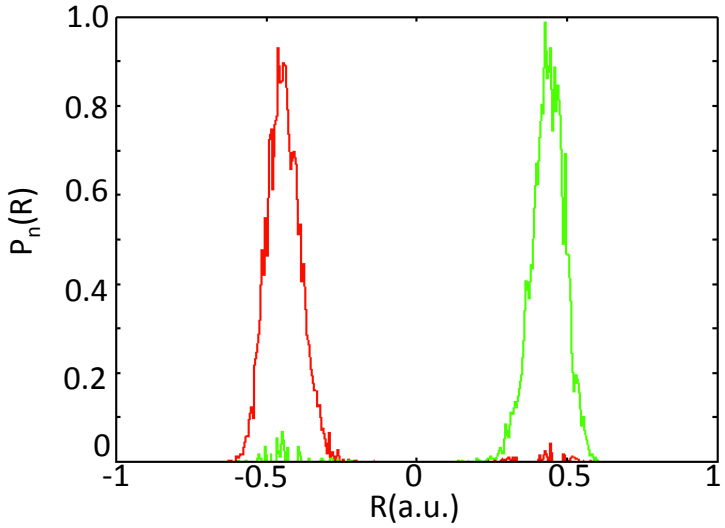

Figure 3.5: State-specific proton histogram for concerted two state coupled to proton double well model

den of bead convergence would decrease in a full state space representation of our PCET system. The next section discusses how to represent the mixed state-space electron/position space proton model with four local donor/electron proton states through a quasi-diabatization procedure in concerted and sequential model systems.

3.3 Summary

In this chapter we discussed two models for condensed phase PCET reported in the literature. The first is comprised of capped Coulombic wells coupled to a proton double well potential. In the RPMD framework, Miller and coworkers represented the electronic and proton with distinct position-space ring polymers. While this works well at capturing PCET rates across multiple regimes, it treats electrons and protons as distinguishable particles and is limited to sin-

gle proton/electron processes. The next model moves towards representing a broader range of PCET systems by treating the electron with discrete ET states in the MV-RPMD framework. The treatment of discrete ET states with continuous electronic conjugate variables solves the issue of treating the electron as a distinguishable particle and is generalizable to multi-electron processes. There are still two shortcomings to the mixed PCET representation. The first is that the proton is still being treated as a distinguishable particle and the model system is limited to single proton processes. Further, the position-space RP representation of the proton, imposes an unnecessary numerical demand on bead convergence in the mapping variables framework. The $P = 32$ bead requirement is due to the light proton mass while in MV-RPMD, bead convergence with respect to electronic states depend on $\beta\Delta$. Since we work in the nonadiabatic (weak coupling) regime, bead convergence with respect to electronic mapping variables are significantly less demanding. It is then wise to consider moving away from the mixed PCET representation into a more general multi-proton/multi-electron system such as the full state-space representation of PCET. Efforts toward this goal will be the focus of the next section.

CHAPTER 4

SIMULATING PCET WITH MV-RPMD

4.1 Diabatization: Four State electron-proton representation

For each value of the solvent configuration in the range $-6\ a_0 \leq s \leq 6\ a_0$, we diagonalize the system hamiltonian on a uniform DVR grid in the proton coordinate with a grid range of $-2\ a_0 \leq R \leq 2\ a_0$ and 100 grid points. The adiabatic eigenstates obtained upon diagonalizing the system Hamiltonian are writtten as $\langle R; s|\epsilon_i\rangle$ where ϵ_i is the i^{th} adiabatic state with eigenenergy E_i.

Further, by diagonalizing the system Hamiltonian for a single electronic state (donor or acceptor) at each value of s, we construct localized proton wavefunctions, $\langle R; s|l_j\rangle$ where l_j is the j^{th} quasi-diabatic local electron-proton states that can be expressed in terms of the adiabatic eigenstates as,

$$\langle R; s|l_j\rangle = \sum_i \int dR' \langle R; s|\epsilon_i\rangle\langle\epsilon_i|R'; s\rangle\langle R'; s|l_j\rangle \tag{4.1}$$

Matrix elements of the Hamiltonian in the quasi-diabatic basis can then be constructed using

$$\langle l_j|H|l_{j'}\rangle = \sum_{i,i'}\langle l_j|\epsilon_i\rangle\langle\epsilon_i|H|\epsilon_{i'}\rangle\langle\epsilon_{i'}|l'_j\rangle = \sum_i \langle l_j|\epsilon_i\rangle E_i\langle\epsilon_i|l'_j\rangle,$$

where E_i is the energy of the i^{th} eigenstate of the Hamiltonian in Eq. (3.16).

The overlap between the reference quasi-diabatic wavefunction and the adiabatic state for a given value of the solvent coordinate, s, is then obtained by evaluating

$$\langle\epsilon_i|l_j\rangle = \int dR\langle\epsilon_i|R\rangle\langle R|l_j\rangle. \tag{4.2}$$

4.2 PCET Model Systems

Previous work using RPMD for the simulation of PCET in condensed phase model systems used a position-space representation to describe a single distinguishable electron and proton coupled to a thermal bath [51]. Exact quantum dynamics studies [53] and surface hopping based simulations [52] for similar model systems choose to employ a two-state representation of the electron donor and acceptor states coupled to a position space proton. Here, we transform these model Hamiltonians to a representation where four localized, quasi-diabatic electron-proton states are coupled to a thermal bath via a solvent polarization coordinate. The quasi-diabatic states are labeled, DD, DA, AD, and AA following previous literature, where the letters D/A indicate the donor/acceptor state of the particle and the first letter describes the state of the electron while the second letter describes the state of the proton.

Following the quasi-diabatization procedure presented in the previous section we obtain a four-state system-bath PCET Hamiltonian,

$$\begin{aligned} H &= \frac{P_s^2}{2m_s} + \sum_{X,X',Y,Y'=\mathrm{D}}^{\mathrm{A}} |XY\rangle V_{XYX'Y'}(s)\langle X'Y'| \\ &\quad + \sum_j \frac{P_j^2}{2M} + \frac{1}{2}M\omega_j^2(Q_j - \frac{c_j s}{M\omega_j^2})^2. \end{aligned} \tag{4.3}$$

where s, P_s and m_s are the position, momentum, and mass of the solvent polarization coordinate, $V_{XY,X'Y'}(s)$ are the elements of the diabatic potential energy matrix where the subscripts $X/Y/X'/Y' = \{D, A\}$ label the donor and acceptor states of the particles. In Eq. 4.3, P_j, Q_j and M are the momentum, position and mass of the j^{th} bath mode, and c_j is the coupling between the solvent and the

j^{th} bath mode of frequency ω_j. The bath spectral density is Ohmic,

$$J(\omega) = \eta\omega e^{-\omega/\omega_C}, \tag{4.4}$$

with cut-off frequency $\omega_c = \omega_s$ and the dimensionless parameter $\eta/m_s\omega_s$ determines the coupling strength between the solvent and the bath modes [54]. The continuous spectral density is discretized into f oscillators with frequencies [55]

$$\omega_j = -\omega_C \log\left(\frac{j - 0.5}{f}\right), \tag{4.5}$$

and the coupling constants c_j are defined as

$$c_j = -\omega_j\left(\frac{2\eta M\omega_C}{f\pi}\right)^{1/2}, \tag{4.6}$$

where $j = 1, \ldots, f$.

The diagonal elements of the potential energy matrix in Eq. 4.3 obtained through our quasi-diabatization protocol are fitted to quadratic polynomials of the form,

$$V_{XYXY}(s) = as^2 + bs + c \tag{4.7}$$

and the off-diagonal couplings are taken to be constants that are independent of the solvent coordinate.

4.3 State Population Dynamics

For the PCET model systems considered here, the nuclear position vector, $\mathbf{R}_\alpha = (s_\alpha, \mathbf{Q}_\alpha)$, includes both the 1D solvent coordinate coupled to the local electron-proton states and the positions of all the bath modes.

Here, we investigate the mechanism of thermal PCET by initializing trajectories to a non-equilibrium distribution, $\rho_{\text{neq}}(0)$, corresponding to a particular

choice of dividing surface. We then track the electron-proton state population dynamics by evaluating the real-time quantum correlation function,

$$C_{P_n,h}(t) = \mathrm{Tr}\left[\rho_{\mathrm{neq}}(0)\mathcal{P}_n(t)h\right], \tag{4.8}$$

where the Heaviside function, h, is defined in terms of the solvent coordinate and allows us to separately ensemble average over trajectories moving forward (from the dividing surface towards reactants) and backwards (towards products),

$$h = \begin{cases} h(s_t - s^{\ddagger}) & \text{forward} \\ h(s^{\ddagger} - s_t) & \text{backward.} \end{cases} \tag{4.9}$$

In the MV-RPMD framework, the heaviside function in Eq. (4.10) is written in terms of the solvent ring polymer centroid, $h \equiv h(\pm(\bar{s}_t - s^{\ddagger}))$, where $\bar{s} = 1/N \sum_{\alpha=1}^{N} s_\alpha$. The n^{th} state populations at time t are evaluated using the 'Boltzmann' estimator [2, 27],

$$\mathcal{P}_n^{\beta} = \frac{\mathbf{\Gamma}_{nn}}{\mathrm{Tr}[\mathbf{\Gamma}]}, \tag{4.10}$$

where $\mathbf{\Gamma}_{nn}$ is a diagonal element of the matrix previously defined in Eq. (2.57) and the time-evolved positions and momenta are obtained by integrating the MV-RPMD equations of motion in Eq. (2.63).

To initialize trajectories to the dividing surface, we define an initial non-equilibrium density operator, $\rho_{\mathrm{neq}} = \rho_{\mathrm{neq}}^{\mathrm{sys}} \otimes \rho_{\mathrm{eq}}^{\mathrm{bath}}$ where the full system is divided into a relevant subsystem described with non-equilibrium initial conditions and the bath that is initially at equilibrium. The subsystem density matrix is defined by

$$\rho_{\mathrm{neq}}^{\mathrm{sys}} = e^{-\beta H_s}\delta(s - s^{\ddagger}) \prod_{n=1}^{K} \delta(P_n - \mathcal{P}_n^{\ddagger}), \tag{4.11}$$

where H_s is the subsystem Hamiltonian given by the first line of Eq. (4.4), P_n is the population of the n^{th} state, and the solvent position, $s^{\ddagger}$, and electron-proton state populations, $\mathcal{P}_n^{\ddagger}$, together define the dividing surface. Ignoring the

Boltzmann weights associated with each electronic state, we can write the corresponding constraints in the MV-RPMD framework as,

$$\rho_{\text{neq}}^{\text{sys}}(0) = e^{-\beta H_{RP}(s)}\delta(\bar{s}_0 - s^{\ddagger})\prod_{n=1}^{K}\delta(\mathcal{P}_n^{\text{SC}}(0) - \mathcal{P}_n^{\ddagger}), \tag{4.12}$$

where the nuclear ring polymer Hamiltonian is defined in Eq. (2.40) and $\bar{s}_0$ is the nuclear RP centroid constrained to its dividing surface value, $s^{\ddagger}$. Further, in Eq. (4.13), we use the recently derived 'semiclassical' estimator [56],

$$\mathcal{P}_n^{\text{SC}} = \frac{1}{N}\sum_{\alpha=1}^{N}\left[\mathcal{P}_n^{\text{SC}}\right]_{\alpha} = \frac{1}{2N}\sum_{\alpha=1}^{N}([x_\alpha]_n^2 + [p_\alpha]_n^2 - 1), \tag{4.13}$$

where $\left[\mathcal{P}_n^{\text{SC}}\right]_{\alpha}$ is the state population associated with the α^{th} bead. We note that this population estimator was rigorously derived in the context of MV-RPMD to yield the exact equilibrium populations at time $t = 0$ [56], and is of similar form to the original semiclassical population function [57, 58]. The present bead-averaged form in Eq. (4.14)has also been used as an estimator in the Nonadiabatic-RPMD method where trajectories are initialized to an exact equilibrium path-integral distribution and time-evolved under the semiclassical mapping Hamiltonian [59]. Finally, it is important to recognize that constraining electronic state populations via $\mathcal{P}_n^{\text{SC}}$ in the correlation function in Eq. (4.12), does not constrain $\mathcal{P}_n^{\beta}$ to the same values at $t = 0$ since the latter includes the correct Boltzmann weights for each electronic state at a given nuclear configuration. For each model, we calculate the real-time correlation function in Eq. (4.9) by sampling the initial nuclear and electronic non-equilibrium distribution using Path Integral Monte Carlo (PIMC). The initial electronic state population variables should be sampled subject to the bead-average constraint described in Eq. (4.12). However, following previous work [27], we implement this constraint by setting *individual* bead state populations to the desired values at the

dividing surface rather than constraining the average,

$$\left[\mathcal{P}_n^{\mathrm{SC}}\right]_\alpha = \mathcal{P}_n^{\ddagger}. \tag{4.14}$$

In the next section we discuss the simulation details for equilibrium and dynamics for concerted and sequential PCET models.

4.4 Concerted PCET

4.4.1 Equilibrium

The parameters for the concerted model are reported in the appendix (A.2). We use PIMC to generate state-specific solvent histograms shown in Fig. (4.1). We used 1×10^8 MC point to achieve equilibrium convergence.

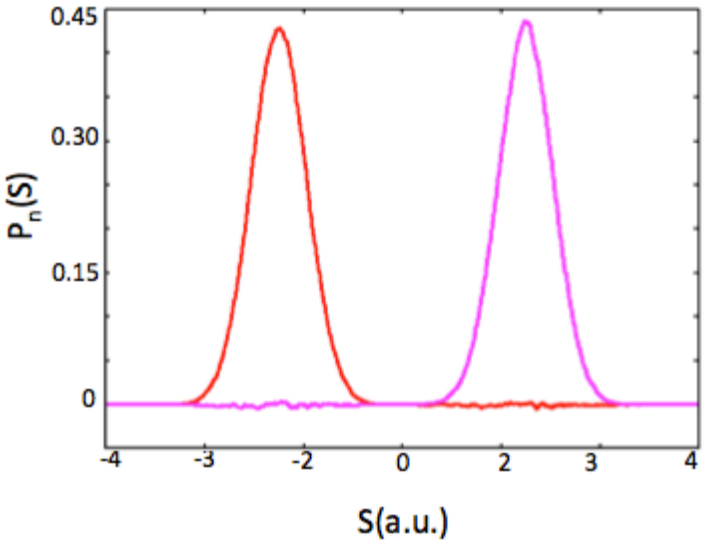

Figure 4.1: State-specific solvent histogram for concerted four state model

We show bead convergence for the concerted model in Fig. (4.2). Average

energy bead convergence is established with 5 beads and error bars are on the order of 10^{-5}. Similarly we achieved bead convergence for the sequential ET-PT and PT-ET models systems. The parameters for these models are also reported in the appendix (A.2). We note that in these systems, due to ET and PT being in weak coupling regime, we establish convergence with significantly fewer beads in the full state-space representation compared to the mixed position-space proton/discrete electronic state representation which would require a $P = 32$ bead calculation.

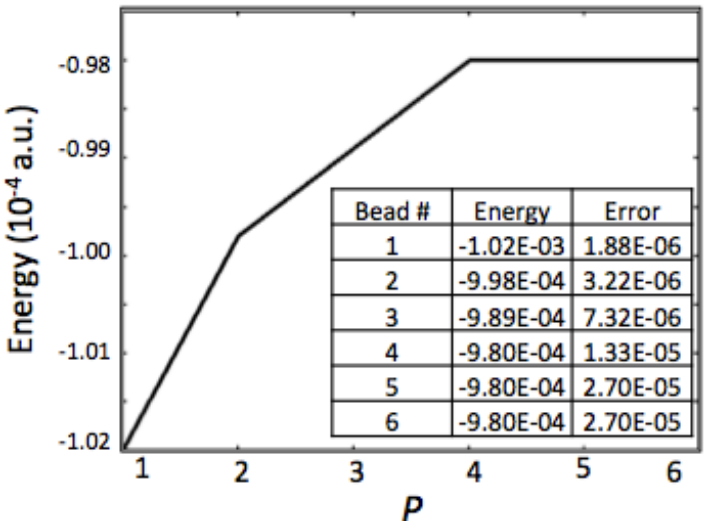

Bead #	Energy	Error
1	-1.02E-03	1.88E-06
2	-9.98E-04	3.22E-06
3	-9.89E-04	7.32E-06
4	-9.80E-04	1.33E-05
5	-9.80E-04	2.70E-05
6	-9.80E-04	2.70E-05

Figure 4.2: Average energy bead convergence

4.4.2 Dynamics

The dividing surface in model I is chosen to be the intersection of the reactant (DD) and product (AA) quasi-diabatic state potentials such that $s^{\ddagger} = 0$ a.u. and only the DD and AA states are populated with $\mathcal{P}^{\ddagger}_{\mathrm{DD}} = \mathcal{P}^{\ddagger}_{\mathrm{AA}} = 0.5$ and

$\mathcal{P}^{\ddagger}_{\mathrm{DA}} = \mathcal{P}^{\ddagger}_{\mathrm{AD}} = 0$. We sample the distribution with a total of 5×10^8 MC points and bead convergence is achieved with $N = 10$ beads.

For model I, MV-RPMD trajectories initialized to the dividing surface are propagated using a 4^{th} order Adams-Bashforth-Moulton predictor corrector integrator with a time step of size 10^{-2} fs. Trajectories were integrated for a total simulation time of 500 fs for models I. The number of trajectories used to obtain the converged results shown below were 2.5×10^4.

We separate the ensemble of trajectories into a group that moves 'forward' towards product formation (increasing values of the solvent coordinate) and a group that moves 'backward' towards the reactant state (decreasing values of the solvent coordinate) to obtain the correlation function $C_{P_n,h}(t)$ defined in Eq. (4.9). Splicing the forward and backward averages together at time zero, we obtain the population plots shown here.

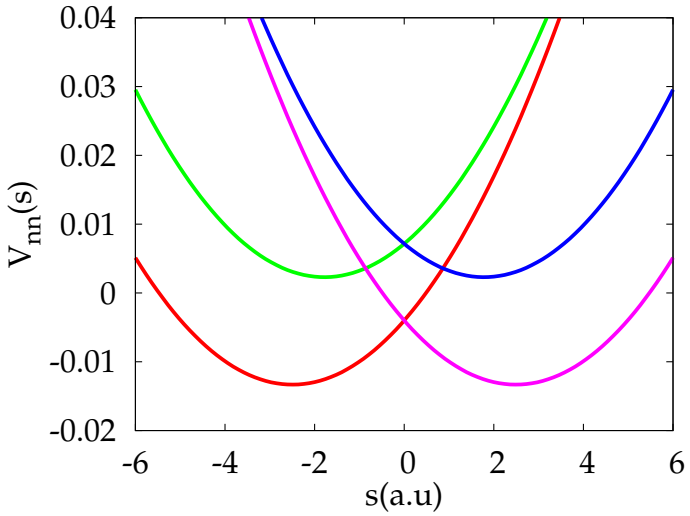

Figure 4.3: The quasi-diabatic state potentials as a function of solvent coordinate are shown for model I, with state DD in red, DA in green, AD in blue, and AA in pink.

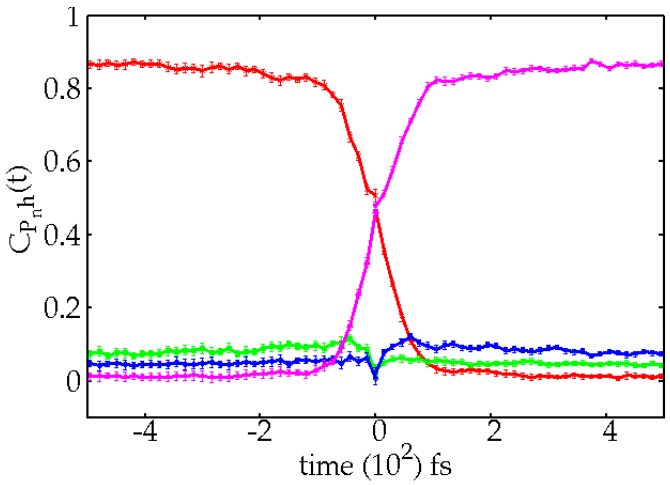

Figure 4.4: Population dynamics for model I (concerted), where population transfers directly from the reactant DD state (in red) to product AA state in pink. The intermediate AD (in blue) and DA (in green) states are not populated during the course of the reaction.

The diabatic potential energy surfaces as a function of the solvent coordinate for model I are shown in Fig. 4.3, and the corresponding population dynamics are shown in Fig. 4.4. Reading the plot chronologically from left to right, we find the initially populated reactant state (DD) where both electron and proton are in the donor state transfers population to the product state (AA) where both the electron and proton are in the acceptor state. This indicates a concerted PCET mechanism where the proton and electron transfer simultaneously on a sub-picosecond time scale. The energetically unfavorable AD and DA states are not involved in the PCET process, but we find a small population in both states that decays to zero at long times.

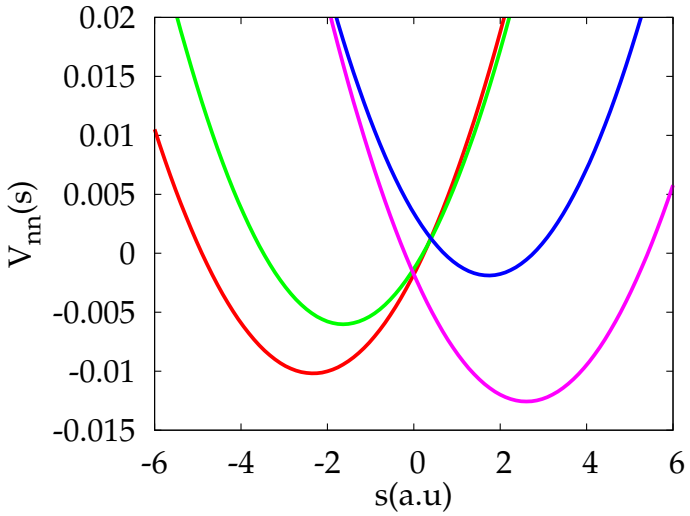

Figure 4.5: The quasi-diabatic state potentials as a function of solvent coordinate for model II with state DD in red, DA in green, AD in blue, and AA in pink.

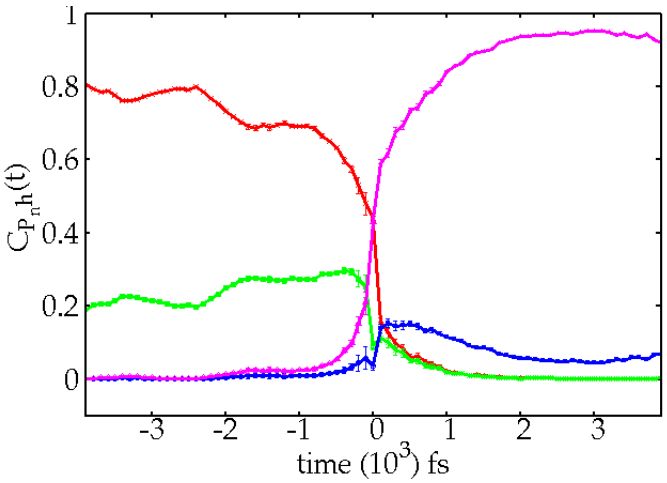

Figure 4.6: Population dynamics for model II (sequential PT-ET), where population first transfers from the reactant DD state (in red) to the DA state (in green) corresponding to proton transfer before the electron transfers leading to a rapid rise in the population of the product AA state in pink.

4.5 Sequential PT-ET

4.5.1 Dynamics

The dividing surface for model II is chosen to be the intersection of the reactant (DD) and product (AA) quasi-diabatic state potentials such that $s^{\ddagger} = 0$ a.u. and

only the DD and AA states are populated with $\mathcal{P}^{\ddagger}_{\mathrm{DD}} = \mathcal{P}^{\ddagger}_{\mathrm{AA}} = 0.5$ and $\mathcal{P}^{\ddagger}_{\mathrm{DA}} = \mathcal{P}^{\ddagger}_{\mathrm{AD}} = 0$. We sample the distribution with a total of 5×10^8 MC points and bead convergence is achieved with $N = 10$ beads.

For model II, MV-RPMD trajectories initialized to the dividing surface are propagated using a 4^{th} order Adams-Bashforth-Moulton predictor corrector integrator with a time step of size 10^{-2} fs. Trajectories were integrated for a total simulation time of 3000 fs. The number of trajectories used to obtain the converged results shown below were 8×10^4.

We separate the ensemble of trajectories into a group that moves 'forward' towards product formation (increasing values of the solvent coordinate) and a group that moves 'backward' towards the reactant state (decreasing values of the solvent coordinate) to obtain the correlation function $C_{P_n,h}(t)$ defined in Eq. (4.9). Splicing the forward and backward averages together at time zero, we obtain the population plots shown here.

We plot the diabatic potential energy surfaces for model II in Fig. 4.5 and the corresponding MV-RPMD population dynamics plotted in Fig. 4.6. Again, reading the plot chronologically, we find that both the reactant (DD) state and the DA (proton transfer only) state are populated although the monotonic trend indicates that at sufficiently long times $t \to -\infty$ the *DD* state will be fully populated and the *DA* state will have zero population.

In Fig. 4.6, we see additional population transfer from the DD to DA state on a timescale of $\approx$ 200 fs preceding the rise in the product (AA) state population. We also note a negligible population transfer from the DA to AD state at short times that decays into thermal population in the AD state at longer times.

These results thus suggest a sequential mechanism for PCET where the proton transfers first, facilitating electron transfer.

4.6 Sequential ET-PT

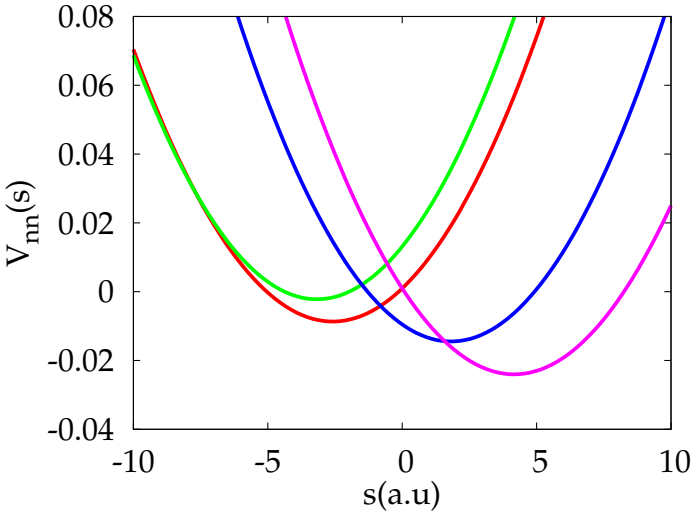

Figure 4.7: The quasi-diabatic state potentials as a function of solvent coordinate are shown for model III, with state DD in red, DA in green, AD in blue, and AA in pink.

4.6.1 Dynamics

The dividing surface for model III chosen to be the intersection of the reactant (DD) and product (AA) quasi-diabatic state potentials such that $s^{\ddagger} = 0$ a.u. and only the DD and AA states are populated with $\mathcal{P}^{\ddagger}_{\mathrm{DD}} = \mathcal{P}^{\ddagger}_{\mathrm{AA}} = 0.5$ and $\mathcal{P}^{\ddagger}_{\mathrm{DA}} = \mathcal{P}^{\ddagger}_{\mathrm{AD}} = 0$. We sample the distribution with a total of 5×10^8 MC points and bead convergence is achieved with $N = 10$ beads.

For model III, MV-RPMD trajectories initialized to the dividing surface are propagated using a 4^{th} order Adams-Bashforth-Moulton predictor corrector integrator with a time step of size 10^{-2} fs. Trajectories were integrated for a total

simulation time of 500 fs. The number of trajectories used to obtain the converged results shown below were 1.5×10^5.

We separate the ensemble of trajectories into a group that moves 'forward' towards product formation (increasing values of the solvent coordinate) and a group that moves 'backward' towards the reactant state (decreasing values of the solvent coordinate) to obtain the correlation function $C_{P_n,h}(t)$ defined in Eq. (4.9). Splicing the forward and backward averages together at time zero, we obtain the population plots shown here.

The diabatic potential energy surfaces for model III is shown in Fig. 4.7 and the corresponding population dynamics in Fig. 4.8. We find that the system is initially in the reactant DD state with significant thermal population the DA state. Following the dynamics we find, however, that unlike model II population transfers from the reactant state to the AD state corresponding to electron transfer preceding the rise in population of the product AA state. This indicates a sequential PCET mechanism where the electron transfers first facilitating proton transfer.

4.7 Alternate Dividing Surface: Sequential ET-PT

4.7.1 Dynamics

Finally, we use model III to demonstrate that the mechanism predicted by MV-RPMD is independent of the choice of initial dividing surface We choose a different dividing surface with $s^\ddagger = -0.8$ a.u. (at the intersection of the

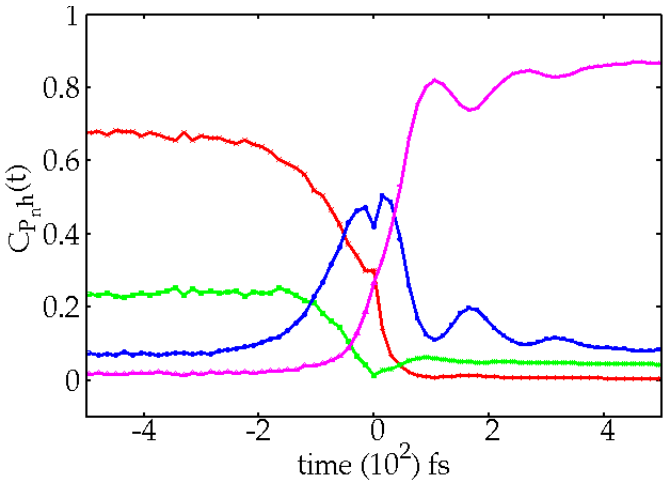

Figure 4.8: Population dynamics for model III (sequential ET-PT), where population first transfers from the reactant DD state (in red) to the AD state (in blue) corresponding to electron transfer before the proton transfers leading to a rapid rise in the population of the product AA state in pink. The DA state (in green) shows some initial thermal population but is not populated during the course of the reaction.

DD and AD states) and the initial electronic state populations are taken to be $\mathcal{P}^{\ddagger}_{\mathrm{DD}} = \mathcal{P}^{\ddagger}_{\mathrm{AD}} = 0.5$ and $\mathcal{P}^{\ddagger}_{\mathrm{DA}} = \mathcal{P}^{\ddagger}_{\mathrm{AA}} = 0$. For this simulation, trajectories were integrated for a total time of 500 fs and 2.5×10^4 trajectories were employed to obtain the converged results shown here.

Despite initializing MV-RPMD trajectories to the same initial dividing surface for all three models, we find population dynamics point to three different PCET mechanisms. Here we show that MV-RPMD simulations can yield mechanistic insights independent of the initial choice of dividing surface for the reactive trajectories by using a different dividing surface in model III. In Fig. 4.9 we plot the results of this simulation where the initial dividing surface is chosen to be at the intersection of the reactant DD state and the electron-transfer only AD state. We find the predicted mechanism is unchanged —population transfer from the reactant state to the AD state first, before PCET product formation.

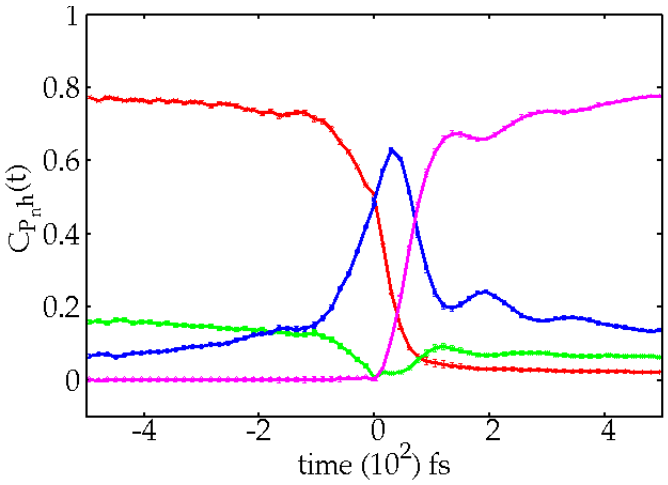

Figure 4.9: Population dynamics for model III (sequential ET-PT), with reactant state in red, PT state in green, ET in blue and product state in pink where trajectories are initialized to the electron transfer transition state.

4.7.2 Verification with Rate Theories

We verify the accuracy of the PCET mechanism predicted by the MV-RPMD simulation by calculating Fermi's Golden Rule (FGR) rates for concerted PCET, electron-transfer, and proton-transfer for each model [60]. For Models I and III, the electron transfer is near-adiabatic and we use Kramer's rate theory [61] to calculate rates for these processes.

We estimate the FGR rate using a simple analytical form derived for systems in which the reactant and product diabatic potential energy surfaces are displaced harmonic oscillators with frequency ω and coupling Δ [62],

$$k_{\mathrm{FGR}} = \frac{2\pi}{\hbar\omega}|\Delta|^2 e^{vz-S}\,\mathrm{coth}^{(z)} I_v\left(S\ \mathrm{csch}\,(z)\right), \tag{4.15}$$

where $\omega = \sqrt{2a/m_s}$ is the frequency of the product diabatic state, $v = (V_R - V_P)/\omega$, $z = \beta\omega/2$, $S = m_s\omega V_d^2/2\hbar$, I_v is a modified Bessel function of the first kind, V_d is the horizontal displacement of the diabatic potential energy functions, and $V_{R/P}$ are the values of the potential energy at the reactant/product minimum such that

Reaction Path	Model I	Model II	Model III
$k_{\mathrm{DD}\to\mathrm{AA}}$	$\mathbf{1.85 \times 10^{7}}$	1.61×10^{6}	4.70×10^{6}
$k_{\mathrm{DD}\to\mathrm{DA}}$	9.81×10^{-17}	$\mathbf{2.53 \times 10^{9}}$	5.97×10^{4}
$k_{\mathrm{DD}\to\mathrm{AD}}$	$2.69 \times 10^{5^{*}}$	1.01×10^{6}	$\mathbf{1.03 \times 10^{11}}^{*}$

Table 4.1: FGR and Kramer's theory rates (indicated with a *) for concerted PCET ($k_{\mathrm{DD}\to\mathrm{AA}}$), electron transfer ($k_{\mathrm{DD}\to\mathrm{AD}}$), and proton transfer ($k_{\mathrm{DD}\to\mathrm{DA}}$) from the reactant DD state for all three models are reported in s^{-1}. The fastest rate for each model is highlighted in bold to indicate the preferred mechanism.

$V_R - V_P$ measures the driving force. For adiabatic ET, we use Kramers theory, [61]

$$k_{\mathrm{KT}} = \left(\sqrt{1 + \left(\frac{\gamma}{2\omega_b} \right)^2} - \frac{\gamma}{2\omega_b} \right) \frac{\omega}{2\pi} e^{-\beta G^{\ddagger}_{\mathrm{cl}}}, \tag{4.16}$$

where ω_b is the frequency at the top of the barrier, $G^{\ddagger}_{\mathrm{cl}}$ is the solvent FE barrier when the solvent is treated classically, and $\gamma = \eta/M_S$. [63] The resulting rates are reported in Table and as expected we find that the fastest rate for model I corresponds to a concerted PCET reaction, for model II the proton transfer reaction is the most rapid and for model III the electron transfer reaction rate is the fastest.

4.8 Summary

We have extended the applicability of MV-RPMD to the simulation of condensed phase PCET using an improved formalism and a new population estimator to follow state to state population transfer dynamics. We employed a simple quasi-diabatization procedure to build three model PCET systems where four local electron-proton states are coupled to a thermal bath via a single solvent polarization coordinate. Following the population dynamics by initial-

izing MV-RPMD trajectories to an arbitrary dividing surface we identify the mechanism of PCET for each of the three models and verify the accuracy of the predicted mechanism against FGR and Kramer's rate theory predictions. By performing a simulation with a different dividing surface, we were also able to clearly establish that our MV-RPMD simulations yield mechanisms that are independent of the initial choice of dividing surface to which trajectories are constrained.

The direct dynamic simulation techniques presented here can be readily extended to future studies of complex photochemical reactions and particularly photo-initiated PCET processes in the condensed phase. Future work in this direction will include deriving a systematic correction to the approximate MV-RPMD dynamics. In addition, we recognize that accurately parameterizing a system-bath Hamiltonian of the form described in Appendix from an atomistic simulation remains a significant challenge.

CHAPTER 5

MV-RPMD RATE THEORY

5.1 Semiclassical Instanton Theory

There are two versions of the semiclassical instanton rate theories. The first is derived from the exact quantum flux-side correlation function. For a 1-D system, the rate expression for the first approach is ,

$$k_{\text{inst}}Z = (2\pi\hbar^3)^{-1/2}\left|\frac{d^2\bar{S}}{d\beta^2}\right|^{1/2}\exp(-\bar{S}/\hbar) \tag{5.1}$$

where $\beta = 1/kT$, Z is the reactant partition function, and $\bar{S}$ is the classical action along the "instanton" trajectory. The trajectory is a period orbit in the inverted potential with a period $\beta\hbar$. Below the "cross-over" temperature $T_c = 1/k\beta_c$, with $\beta_c = 2\pi/\hbar\omega_b$ and ω_b is the barrier frequency, one or more periodic orbits can form.

The second, which is sometimes called the "ImF" method, is obtained by modeling the rate of transmission through a barrier with the rate of decay of the thermal average of shape resonances through the barrier. The method gives a rate expression with an exponent containing the action of the instanton, but a different prefactor. The rate expression is given by,

$$kZ_r \approx \frac{2}{\beta\hbar}\text{Im}R \tag{5.2}$$

where,

$$R = \sum_k e^{-\beta(E_{\mathbf{r}_k} - i\gamma_k/2)} \tag{5.3}$$

Upon performing the analytic continuation of the Hamiltonian $\hat{H}$ into the complex plane, we obtain the discrete spectrum described by the set of complex numbers $E_{\mathrm{r}k} - i\gamma_k/2$. Deriving the instanton theory involves a combination of steepest descent and analytic continuation applied to the exact expression for Z_r.

The first approach is typically preferred as it is more mathematical rigorous, but in the "ImF" approach the connection of instanton theory to RPMD becomes apparent. The following sections will give a brief review of both methods.

5.2 Miller-Schwartz-Tromp Flux-side TCF

We start our derivation of the flux-side rate expression by considering the collinear reaction A + BC $\rightarrow$ AB + C, where the initial arrangement A + BC is denoted by "a" and the final arrangement is denoted by "b". The rate can be expressed as the sum over the Boltzmann average of initial vibrational states and translational energy [64, 65],

$$k_{a\rightarrow b} = (2\pi\mu kT)^{(-1/2)} Q_{BC}^{-1} \sum_{\eta_a,\eta_b} \int_0^\infty dE_1 e^{-\beta(E_1+\epsilon_{\eta_a})} |S_{\eta_a,\eta_b}(E_1)|^2 \tag{5.4}$$

where $\beta = 1/kT$, μ is the reduced mass for the initial arrangement "a", η_a and η_b are the vibrational quantum numbers of BC and AB respectively, E_1 is the initial translational energy, and $|S_{\eta_a,\eta_b}(E_1)|^2$ is the S scattering matrix for the reactive process. The vibrational partition function of BC is,

$$Q_{BC} = \sum_{\eta_a} e^{-\beta\epsilon_{\eta_a}} \tag{5.5}$$

where ϵ_{η_a} are the vibrational energy levels of BC. In order to recast Eq. (5.4) into a more convenient form, we can introduce the notion of flux through a surface

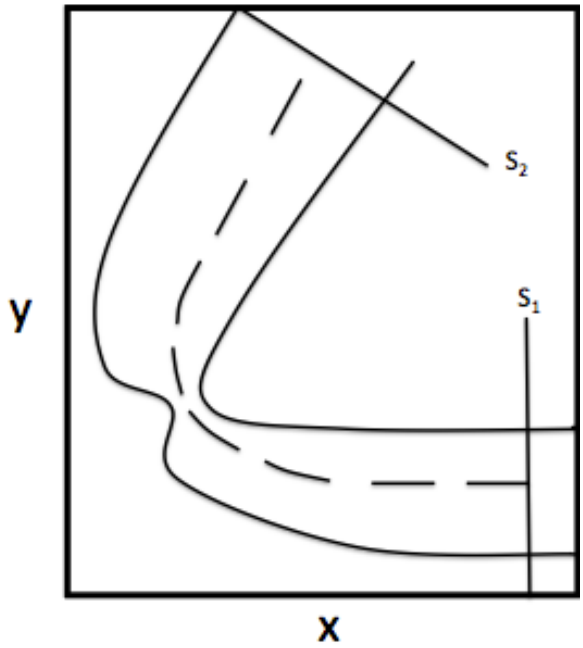

Figure 5.1: Sketch of collinear potential energy surface forA+BC → AB+C.

[66]. In Figure (5.1), x and y are mass weighted or skewed reaction coordinates that diagonalize the kinetic energy: $x = R(\mu/M)^{1/2}$, $y = r(m/M)^{1/2}$. R and r are the transitional and vibrational coordinates, respectively and μ and m are the reduced masses [(m=BC/(B+C), μ= A(B+C)/(A+B+C)]. M is an arbitrary mass, with a corresponding classical kinetic energy $\frac{1}{2}M(\dot{x}^2 + \dot{y}^2)^2$ and s and u in the figure are linear combinations of x and y which diagonalize the potential energy at the saddle point. S_1, S_2, and S_3 correspond to 1D cuts through the 2D surface which are defined by lines. Consider the first surface, S_1, defined by $R_0 - R = 0$, where R_0 is an asymptotically large value of the coordinate R. The flux through S_1 in terms of the wave function $\Psi(r, R)$ is,

$$-\mathrm{Re}\int_{\infty}^{\infty} dr\Psi(r,R)^{*}\frac{\hbar}{i\mu}\frac{\partial}{\partial R}\Psi(r,R)|R = R_0. \tag{5.6}$$

Here, "Re" denotes "the real part of", and a positive flux is associated with decreasing R, such that flux is chosen to be in the direction of the reaction. The asymptotic form of the scattering solution to the Schrödinger equation, $(H - E)\Psi_{P_1,\eta_a} = 0$, with $E = P_1^2/2\mu$ is,

$$\Psi_{P_1,\eta_a}(r,R) \approx -\frac{\exp(-ik_{\eta_a}R)}{(2\pi\hbar)^{1/2}}\phi_{\eta_a}(r) + \sum_{\eta_a'}\frac{\exp(-ik_{\eta_a'}R)}{(2\pi\hbar)^{1/2}}\phi_{\eta_a'}(r)\left(\frac{v_{\eta_a}}{v_{\eta_a}'}\right)S_{\eta_a,\eta_a'}(E_1) \tag{5.7}$$

where $E_1 = P_1^2/2\mu$ is the initial kinetic energy, $k_n = [2\mu(E-\epsilon_n)]^{1/2}/\hbar$ is the wave number, and $v_n = \hbar k_n/\mu$ is the asymptotic velocity channel. This corresponds to an incident vibrational state η_a. The velocity channel is a normalization for the translational function, which also correspond to delta function normalization on the momentum scale. We can then express the flux in terms of the scattering wave function,

$$-\mathrm{Re}\int_\infty^\infty dr\Psi_{P_1,\eta_a}(r,R)^*\frac{\hbar}{i\mu}\frac{\partial}{\partial R}\Psi_{P_1,\eta_a}(r,R) = v_{\eta_a}(2\pi\hbar)^{-1}\left[1 - \sum_{\eta_a'}|S_{\eta_a,\eta_a'}(E_1)|^2\right]. \tag{5.8}$$

In the asymptotic region of "b", which is the product region, $y = r(m/M)^{1/2}$ is large, which corresponds to large value of the vibrational coordinate of AB. In the region of "b", Ψ_{P_1,η_a}, since it corresponds to an incident wave in arrangement "a", has only outgoing waves such that,

$$\Psi_{P_1,\eta_a}(r,R_b) \approx \sum_{\eta_b}\frac{\exp(-ik_{\eta_b}R_b)}{(2\pi\hbar)^{1/2}}\phi_{\eta_b}(r_b)\left(\frac{v_{\eta_a}}{v_{\eta_b}}\right)S_{\eta_a,\eta_b}(E_1) \tag{5.9}$$

where R_b and r_b are the translational and vibrational coordinates of AB and C respectively. The surface S_2 is defined by $R_0 - R_b$ and the flux through S_2 is,

$$v_{\eta_a}(2\pi\hbar)^{-1}\sum_{\eta_a}|S_{\eta_b,\eta_a}(E_1)|^2. \tag{5.10}$$

Because of unitarity,

$$1 = \sum_{\eta_a'}|S_{\eta_a',\eta_a}(E_1)|^2 + \sum_{\eta_b}|S_{\eta_b,\eta_a}(E_1)|^2 \tag{5.11}$$

we see that the flux through S_1, and S_2 are equivalent. Further the flux through any closed surface is zero which follows from the continuity equation [66],

$$\mathrm{Re} \oint d\mathbf{S} \cdot \Psi^* \frac{\hbar}{i\mu} \nabla \Psi = 0. \tag{5.12}$$

Since S_1, and S_2 can be made into a closed surface by joining the segments at infinity, the flux through S_1, and S_2 must be equal. Writing the flux integral as a volume rather than a surface integral, we can define a surface $f(r, R) = 0$, where $f(r, R) < 0$ corresponds to reactant region of configuration space and $f(r, R) > 0$ corresponds to the product region of configuration space. The flux through this surface written as a volume integral is,

$$\mathrm{Re} \int d\mathbf{q} \delta(f(\mathbf{q})) \Psi^*(\mathbf{q}) \frac{\partial f(\mathbf{q})}{\partial \mathbf{q}} \cdot \mathbf{v} \Psi(\mathbf{q}) \equiv \mathrm{Re} \langle \Psi | F | \Psi \rangle \tag{5.13}$$

where $\mathbf{q} = (r, R)$, and the components of the velocity operator are $v_k = (\hbar / i m_k)(\partial / \partial q_k)$, $k = 1, 2$ and the flux operator is,

$$F = \delta(f(\mathbf{q})) \frac{\partial f(\mathbf{q})}{\partial \mathbf{q}} \cdot \mathbf{v} \tag{5.14}$$

Now we can see that the scattering matrix can be expressed in terms of the real part of the Flux operator in the basis of scattering states,

$$(2\pi\hbar)^{-1} \sum_{\eta_b} |S_{\eta_b, \eta_a}(E_1)|^2 = v_{\eta_a}^{-1} \mathrm{Re} \langle \Psi_{P_1, \eta_a} | F | \Psi_{P_1, \eta_a} \rangle. \tag{5.15}$$

We can then write the expression for the rate as,

$$k_{a \to b} = Q_a^{-1} \sum_{\eta_a} \int_0^\infty dE_1 \exp[-\beta(E_1 + \epsilon_{\eta_a})] v_{\eta_a}^{-1} \langle \Psi_{P_1, \eta_a} | F | \Psi_{P_1, \eta_a} \rangle \tag{5.16}$$

where we take the real part of the right hand side of Eq. (5.16). We also should point out that the flux is independent of the choice of any surface that divides reactants and products, since the flux through any closed surface is the same. Since

$$e^{-\beta H} \Psi_{P_1, \eta_a} = \exp[-\beta(E_1 + \epsilon_{\eta_a})] \Psi_{P_1, \eta_a} \tag{5.17}$$

and,

$$E_1 = P_1^2/2\mu \tag{5.18}$$

$$dE_1 = P_1/\mu dP_1 = v_{\eta_a} dP_1 \tag{5.19}$$

we can rewrite Eq. (5.16) as ,

$$k_{a\to b} = Q_a^{-1} \sum_{\eta_a} \int_{-\infty}^{0} dP_1 \, \langle \Psi_{P_1,\eta_a} | F e^{-\beta H} | \Psi_{P_1,\eta_a} \rangle \tag{5.20}$$

where $P_1 = -(2\mu E_1)^{1/2}$. We can rewrite the integral over all momenta, negative and positive, by inserting a projection operator $\mathcal{P}$ defined by,

$$\begin{aligned} \mathcal{P}\Psi &= \Psi \quad P_1 < 0 \\ \mathcal{P}\Psi &= 0 \quad P_1 > 0 \end{aligned} \tag{5.21}$$

then Eq. (5.20) can be written as

$$k_{a\to b} = Q_a^{-1} \sum_{\eta_a} \int_{-\infty}^{\infty} dP_1 \, \langle \Psi_{P_1,\eta_a} | F e^{-\beta H} \mathcal{P} | \Psi_{P_1,\eta_a} \rangle \tag{5.22}$$

which can be rewritten in terms of the quantum mechanical trace,

$$k = \frac{1}{Q_a} \mathrm{tr}[\hat{F} e^{-\beta \hat{H}} \mathcal{P}] \tag{5.23}$$

and since $\hat{F}$ and $\mathcal{P}$ commute we can write the well known formally exact rate expression as [64, 65],

$$k = \frac{1}{Q_a} \mathrm{tr}[e^{-\beta \hat{H}} \hat{F} \mathcal{P}] \tag{5.24}$$

where $\hat{F}$ is the flux operator defined by,

$$\hat{F} = \delta(s) \frac{p}{m} \tag{5.25}$$

where s and p are the reaction coordinate and momenta respectively. The hamiltonian is,

$$H = \frac{p^2}{2m} + V(s). \tag{5.26}$$

The projection operator, $\mathcal{P}$, is defined in terms of the heaviside in the conjugate momenta,

$$\mathcal{P} = \lim_{t\to\infty} e^{i\hat{H}t/\hbar} h(p) e^{-i\hat{H}t/\hbar} \tag{5.27}$$

where the heaviside function projects onto all states that have positive momentum in the infinite future ($t \to +\infty$). The reaction coordinate direction is defined from $s \to -\infty$ to $s \to +\infty$. Noting that the projection operator, $\mathcal{P}$, is defined in terms of the eigenstates of $\hat{H}$ it's clear that $[\hat{H}, \mathcal{P}] = 0$. We can then rewrite Eq. (5.1) in a more symmetrical form as,

$$k = \frac{1}{Z}\mathrm{tr}[\hat{F} e^{-\beta\hat{H}/2} \mathcal{P} e^{-\beta\hat{H}/2}] \tag{5.28}$$

and with $\mathcal{P}$ given by Eq. (5.4) we can write,

$$k = \lim_{t\to\infty} \frac{1}{Z}\mathrm{tr}[\hat{F} e^{-\beta\hat{H}/2} e^{i\hat{H}t/\hbar} h(p) e^{-i\hat{H}t/\hbar} e^{-\beta\hat{H}/2}] \tag{5.29}$$

5.3 RPMD Rate Theory

It is perhaps not surprising that, since there is an established connection between RPMD and quantum transition state theory, RPMD has successfully been used in the calculation of reaction rates. RPMD's accuracy and efficiency allows for approximate quantum mechanical rate calculations that help inform how certain degrees of freedom within a reactive system contribute to the speed of a reaction. This is promising as we seek to better understand quantum mechanical properties of large scale systems and how knowledge of these properties may inform the design novel materials for a variety of technologies. In 2004 Craig and Manolopolous showed that RPMD can be used to calculate approximate Kubo-transformed flux-side correlation functions of the form [67],

$$\tilde{C}_{fs}(t) = \frac{1}{\beta}\int_0^\beta \mathrm{tr}[e^{-(\beta-\lambda)\hat{H}} \hat{f}(0) e^{-\lambda\hat{H}} e^{+i\hat{H}t/\hbar} \hat{h} e^{-i\hat{H}t/\hbar}] d\lambda \tag{5.30}$$

where $\hat{h} = h[s(\mathbf{q})]$ is a step function that projects onto the product side of the transition state dividing surface at $s(\mathbf{q}) = 0$ and

$$\hat{F} = \frac{i}{h}[\hat{H}, \hat{h}] \tag{5.31}$$

is the reactive flux operator. The reaction rate coefficient can then be written as

$$k = \frac{1}{Z_r} \lim_{t\to\infty} \tilde{C}_{fs}(t) \tag{5.32}$$

where Z_r is the reactant partition function. Since the side operator, $\hat{h}$ is configurational, and the flux operator $\hat{F}$ is not, the RPMD method cannot be applied directly to the Kubo-transformed flux-side correlation function. One remedy is noting that $\hat{F}$ is the Heisenberg derivative of the side operator. We can then calculate the flux-side correlation function equivalently as,

$$\tilde{C}_{fs}(t) = -\frac{d}{dt}\tilde{C}_{ss}(t), \tag{5.33}$$

where $\tilde{C}_{ss}(t)$ is a Kubo-transformed side-side correlation function,

$$\tilde{C}_{ss}(t) = \frac{1}{\beta}\int_0^\beta \mathrm{tr}[e^{-(\beta-\lambda)\hat{H}}\hat{h}(0)e^{-\lambda\hat{H}}e^{+i\hat{H}t/\hbar}\hat{h}e^{-i\hat{H}t/\hbar}]d\lambda \tag{5.34}$$

Since both operators in $\tilde{C}_{ss}(t)$ are configurational, RPMD can be applied and the corresponding approximation to $\tilde{C}_{fs}(t)$ can be obtained upon differentiation $\tilde{C}_{ss}(t)$. Still, there are a few issues to consider in the RPMD approximation to the Kubo-transformed flux-side correlation function. First, the operator $\hat{h}$ is a nonlinear functions of $\hat{\mathbf{q}}$. As mentioned earlier in the discussion on the features of RPMD, RPMD autocorrelation functions involving nonlinear operators having a leading error term $O(t^4)$. This is particularly problematic since we need to calculate the long-time limit of the flux-side correlation function in order to obtain a rate constant, and the method is expected to degrade with time [38]. More worrying, the Kubo-transformed flux-side correlation function has a divergent

first derivative due to the integral over λ. This divergence can be avoided, in an exact calculation, by alternatively using the Miller, Schwartz, and Tromp [65] expression for the flux-side correlation,

$$\tilde{C}_{fs}(t) = \mathrm{tr}[e^{-\beta\hat{H}/2}\hat{F}(0)e^{-\beta\hat{H}/2}e^{+i\hat{H}t/\hbar}\hat{h}e^{-i\hat{H}t/\hbar}] \tag{5.35}$$

which has the same long-time limit as $\tilde{C}_{fs}(t)$ and therefore gives the same reaction rate when substituted into Eq. (5.3). We will note that this is still unsatisfactory since RPMD is an approximation and is limited to Kubo-transformed correlation functions. Nevertheless, RPMD proves to be an accurate approximation to the exact Kubo-transformed flux-side correlation function for standard models of chemical reactions, including a quartic double well coupled to a bath of harmonic oscillators [67]. In fact the RPMD approximation of the Kubo-transformed flux-side correlation function has been shown to give comparable accuracy to the classical Wigner model [68, 69] and centroid molecular dynamics (CMD) [70]. We will now discuss how to express Eq. (5.5) in terms of an RPMD TCF. Consider a d-dimensional system described by the following Hamiltonian,

$$H(\mathbf{p},\mathbf{q}) = \sum_{i=1}^{d}\frac{p_i^2}{2m_i} + V(q_1,\ldots q_d) \tag{5.36}$$

where we define s as the reaction coordinate and the value of the reaction coordinate at the dividing surface that divides reactant and product is $s(q_1,\ldots q_d) = 0$ and $s > 0$ corresponds to the products. The RPMD approximation to the Kubo-transformed side-side correlation function in Eq. (5.5) for a multidimensional harmonic ring polymer is [33],

$$\tilde{C}_{ss}(t) = \frac{1}{(2\pi\hbar)^N}\int d\mathbf{P}_0\int d\mathbf{Q}_0 e^{-\beta_n H_n(\mathbf{P}_0,\mathbf{Q}_0)}h_n(\mathbf{Q}_0)h_n(\mathbf{Q}_t) \tag{5.37}$$

where n is the number of ring-polymer beads, $\beta_n = \beta/n$, and $N = nd$. The Hamiltonian is,

$$H_n(\mathbf{P}_0, \mathbf{Q}_0) = \sum_{i=1}^{d} \sum_{j=1}^{n} \left[\frac{P_{i,j}}{2m_i} + \frac{1}{2} m_i \omega_i (Q_{i,j} - Q_{i,(j-1)})^2 \right] + \sum_{j=1}^{n} V(Q_{1,j}, \ldots, Q_{f,j}), \quad (5.38)$$

and the flux-side TCF in the RPMD representation can be written as

$$\tilde{C}_{fs}(t) \approx \frac{1}{(2\pi\hbar)^N} \int d\mathbf{P}_0 \int d\mathbf{Q}_0 e^{-\beta_n H_n(\mathbf{P}_0, \mathbf{Q}_0)} \delta(\mathbf{Q}_0) v_s(\mathbf{P}_0, \mathbf{Q}_0) h_n(\mathbf{Q}_t) \quad (5.39)$$

where the rate can approximated by,

$$k \approx \frac{1}{Z_r} \lim_{t \to \infty} \frac{1}{(2\pi\hbar)^N} \int d\mathbf{P}_0 \int d\mathbf{Q}_0 e^{-\beta_n H_n(\mathbf{P}_0, \mathbf{Q}_0)} \delta(\mathbf{Q}_0) v_s(\mathbf{P}_0, \mathbf{Q}_0) h_n(\mathbf{Q}_t). \quad (5.40)$$

5.4 ImF and RPMD

The connection of RPMD and semiclassical instant theory arises from the application of the steepest decent approximation and analytic continuation of the ring polymer expression for the partition function. We begin by locating the saddle point on the ring polymer potential surface in the ring polymer Hamiltonian,

$$U_{RP}(R) = \sum_{\alpha=1}^{P} V(R_\alpha) + \frac{mP^2}{2\beta^2\hbar^2} \sum_{\alpha=1}^{P} (R_\alpha - R_{\alpha+1})^2 \quad (5.41)$$

The stationary points of U_{RP} satisfy,

$$V^{'}(R_\alpha) = m \frac{R_{\alpha+1} - 2R_\alpha + R_{\alpha-1}}{(\beta_P \hbar)^2}. \quad (5.42)$$

The solutions correspond to all the normal modes of the ring polymer being zero with the exception of the centroid mode $\bar{R}_0$. The centroid mode is located at the barrier maximum $R^\dagger$. The normal modes Q of a free ring polymer with P beads correspond to the eigenstates of a P-member cyclic Huckel system. For

an even number of beads the normal modes are given by,

$$Q_0 = \frac{1}{P}\sum_{\alpha=1}^{P} R_\alpha, \tag{5.43}$$

$$Q_k = \left(\frac{2}{P}\right)^{1/2}\sum_{\alpha=1}^{P}\sin\left(\frac{2\alpha k\pi}{P}\right)R_\alpha, \quad k = 1,\ldots,(P-2)/2 \tag{5.44}$$

$$Q_{-k} = \left(\frac{2}{P}\right)^{1/2}\sum_{\alpha=1}^{P}\cos\left(\frac{2\alpha k\pi}{P}\right)R_\alpha, \quad k = 1,\ldots,(P-2)/2 \tag{5.45}$$

$$Q_{P/2} = \frac{1}{P}\sum_{\alpha=1}^{P}(-1)^P R_\alpha, \tag{5.46}$$

For an odd number of beads the last mode is omitted. The frequencies corresponding to each normal mode are

$$\omega_{\pm k} = \frac{2P}{\beta\hbar}\sin\left(\frac{|k|\pi}{P}\right). \tag{5.47}$$

Further, the normal mode frequencies satisfy

$$\omega_{\pm k} =\approx 2|k|\pi/\beta\hbar \tag{5.48}$$

for low values of k and as $P \to \infty$. The solutions for the free RP corresponds to all normal modes being zero except for the centroid which is located at the barrier maximum $R^\dagger$. Above the cross-over temperature, T_c, the geometry at the barrier $R^\dagger$ is the saddle point on $U_{RP}(R)$, which is equivalent to the dynamics of the ring polymer in classical limit where the ring polymer collapses to a single point. Below T_c , $U_{RP}(R)$ changes the geometry of R_α such that it is no longer a saddle point. Above the crossover temperature, T_c the normal mode frequencies $\sqrt{\omega_k^2 = \omega_b^2}$ are real except for the imaginary frequency, $i\omega_b$ corresponding to the centroid mode. Below T_c the normal mode frequencies ($\omega_{\pm 1} < \omega_b$), so the modes are no longer stable and the geometry $R_P = R^\dagger$ has three imaginary frequencies. The unstable modes, $Q_{\pm 1}$ describe the RP lowering its energy by ”draping” over the barrier.

The physical interpretation of the saddle point below the critical temperature corresponds to a finite-difference approximation to Newton's second law, describing the classical dynamics of a particle on an inverted potential surface $-V(R)$. Each bead in the RP corresponds to equally spaced imaginary time-steps with a duration of $\beta\hbar$. It then follows that the saddle point is a finite difference approximation to the periodic instanton trajectory. The instanton rate is calculated by computing the normal modes and frequencies of the RP at the saddle point by diagonalizing the Hessian. The next step is to multiply the RP coordinates by complex scaling factors in order to transform the partition function, which is real and infinite, into the R term in Eq. (5.2) which is finite and complex. Finally computing the integrals over the normal modes using steepest descent gives the RP form of the ImF instanton rate. This can be expressed as,

$$\mathrm{Im}R = \frac{P\sqrt{B_P}}{2}\Big(\frac{m}{2\pi\beta_P\hbar^2}\Big)^{p/2} e^{-\beta_P U_P} \prod_{k=0}^{P-1} \int dQ_k e^{\beta_P m \eta_k^2 Q_k^2/2}, \tag{5.49}$$

where Q_k and η_k are the normal modes and frequencies respectively. Evaluation of the gaussian integrals and substituting in Eq (5.2) yields the following expression for the instanton rate,

$$k_{\mathrm{inst}} Z_r = A_P(\beta) e^{-\beta_P U_P} \tag{5.50}$$

where

$$A_P(\beta) = \frac{1}{\beta_P\hbar}\sqrt{\frac{m\beta_P}{2\pi\beta_P\hbar^2}}\Big|\prod_{k=0}^{P-1}\hbar\eta_k\beta_P\Big|^{-1}. \tag{5.51}$$

This expression tends to the standard "ImF" form of the instanton rate in the limit $P \to \infty$, where $\beta_P U_P$ is the classical action $S/\hbar$ along the instanton trajectory. The connection to RPMD rate theory is given by first considering the constrained partition function in terms of the free energy F,

$$Z = \int du e^{-\beta F(u)} \tag{5.52}$$

where the free energy, $F(u)$ is,

$$F(u) = -\frac{1}{\beta}\ln[Z_{\sigma=u}] \tag{5.53}$$

and $Z_{\sigma=u}$ is the constrained partition function,

$$Z_{\sigma=u} = \frac{1}{(2\pi\hbar)^P}\int d\mathbf{P}\int d\mathbf{R}e^{-\beta_P H_P(\mathbf{P},\mathbf{R})}\delta(\sigma(\mathbf{R})-u) \tag{5.54}$$

where $\sigma(\mathbf{R})$ is the unstable degree of freedom for which the evaluation of the integral over the free energy can be accurately approximated using steepest decent about $u = 0$. Integrated over u and making the steepest decent approximation we obtain,

$$\mathrm{Im}R = \sqrt{\frac{\pi}{2\beta|F''(0)|}}\frac{1}{(2\pi\hbar)^P}\int d\mathbf{P}\int d\mathbf{R}e^{-\beta_P H_P(\mathbf{P},\mathbf{R})}\delta(\sigma(\mathbf{R})-u). \tag{5.55}$$

5.5 Finding the MV-RPMD Instanton

In the previous section we discussed RPMD's connection to semiclassical instanton theory. Namely, we saw that the RPMD instanton is a classical path that minimizes the action along the reaction coordinate. This corresponds to a periodic orbit on an inverted potential with period $\beta\hbar$. In order to calculate the RPMD instanton one needs to compute the normal modes at the saddle point by diagonalizing the Hessian of the RP Hamiltonian [3, 71, 72, 73]. The unstable mode, or the transition state, will correspond to the eigenvector with the negative eigenvalue. The next step is to use a combination of complex scaling, where we multiply the unstable mode by $i = \sqrt{-1}$ for values greater than zero, and steepest descent to evaluate the integrals over all modes [71, 72, 73]. Doing so will give an expression, which in the limit of a large bead number, gives the "ImF" form of the instanton rate which is exact for a harmonic barrier.

With our goal being the development of a nonadiabatic rate theory in the MV-RPMD formalism, it is of interest to apply the above technique to MV-RPMD, in order to find the instanton configuration for nonadiabatic systems. This is done by diagonalizing the Hessian of the MV-RPMD Hamiltonian and finding the unstable mode (eigenvector with a negative eigenvalue) along the MV-RPMD potential surface. Following these prescriptive measures, nonadiabatic instanton configurations have been reproduced for a two-state spin-boson model in the weak and strong coupling regime in both nuclear and electronic degrees of freedom [74].Despite this, current optimization algorithms are not generalizable to systems with a large number of states. It is then wise to turn to other methods for calculating high-dimensional nonadiabatic instanton configurations.

Another method to consider, due to its classical scaling and efficiency in practice, is exact PIMC calculations in MV-RPMD framework. Using PIMC we can calculate average instanton configurations in both nuclear and electronic degrees of freedom. Being that PIMC is an exact quantum statistics method, and the instanton is an imaginary-time periodic path around the reaction barrier, PIMC in the MV-RPMD framework should be able to generate exact instanton configurations. The next section will discuss some preliminary results working toward this goal.

5.6 Averaging Algorithm

The first step in calculating the MV-RPMD instanton is to consider the issue of artificially labeling beads in the calculation of average bead configurations. In

order to circumvent this issue we devise an algorithm that post processes RP equilibrated configurations such the first bead has the most positive solvent polarization value. We begin by initializing the PIMC simulation such that the ring polymer beads are randomly distributed about the crossing. Upon generating sufficient electronic and nuclear configurations we arrange the nuclear RP beads such that the first bead, which we arbitrarily label as "bead 1", has the most positive nuclear position value. We then reorder the remaining nuclear beads such that the contiguous order of the remaining $P-1$ beads are retained. We then order the remaining electronic conjugate variables according to the nuclear instanton bead ordering.

5.7 Equilibrium Simulation Results

For our instanton configuration calculations we use a simple two-state model described by the Hamiltonian [4]

$$H = \frac{1}{2}m\dot{S}^2 + \Delta\sigma_x + \frac{1}{2}m\omega_2(S - \sigma_z S_0)^2 \tag{5.56}$$

where σ is the Pauli spin matrix, and Δ is the adiabatic coupling. The parameters are chosen to be $\omega = 1.0$, $m = 1.0, \beta = 5.0$ and $S_0 = 5.0$. This corresponds to two-state system defined in terms of a solvent polarization coordinate. We establish convergence with 1×10^8 Monte Carlo points for each bead simulation.Figure (5.2) shows the average energy, given by the Eq. (2.6), as a function of MC points. We establish average energy bead convergence with 12 bead to get $\langle E \rangle$ = 6.5a.u. We find the instanton path corresponding to this system to be in qualitative agreement with the exact quantum instanton calculation reported by Cao and Voth [4]. Disappointingly, our method of averaging instantaneous

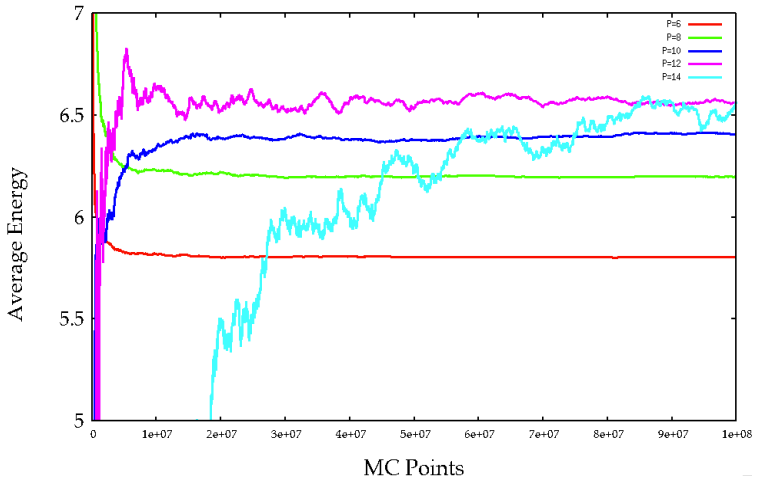

Figure 5.2: Average energy bead convergence as a function of MC points

instanton configurations introduces arbitrary discrepancies in which bead assumes the minimum value in individual instanton configurations. This causes the average minimum value to be located slightly above the minimum value reported by Cao and Voth [4]

We also calculate the average semiclassical population for this system and plot each bead population throughout the course of the MC simulation. As the simulation approaches convergence with respect to the number of MC points the population of state 1 (shown in red in Fig. 5.4) and the population of state 2 (shown in green in Fig 5.4) approach equality. This suggests that constraining the ring polymer centroid to the barrier constrains the average electronic population of each bead to be equal.

In order to demonstrate why the minimum value of the averaged instanton configuration is slightly greater than the reported value, we plot instantaneous

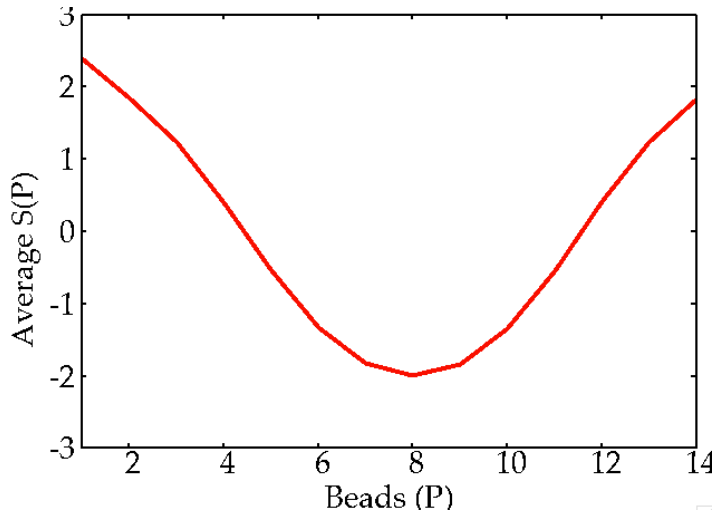

Figure 5.3: The nonadiabatic instanton trajectory plotted as a function of imaginary time

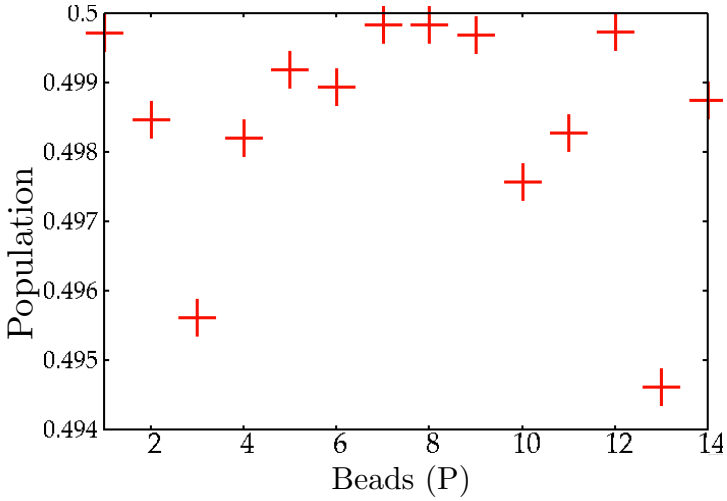

Figure 5.4: Average Semiclassical Population with the population of state 1 (shown in red) and state 2 (shown in green) over the course of the MC simulation

instanton configurations in Fig (5.5). As mentioned before, the arbitrary choice of making the ”bead 1” have the maximum value causes discrepancies in which

bead number assumes the minimum value in each instantaneous instanton configuration. The bead number with minimum value shifts between bead 6-10 causing bead 8 (which should have the minimum value) to be on average at a position slightly greater than the minimum value reported by Cao and Voth.

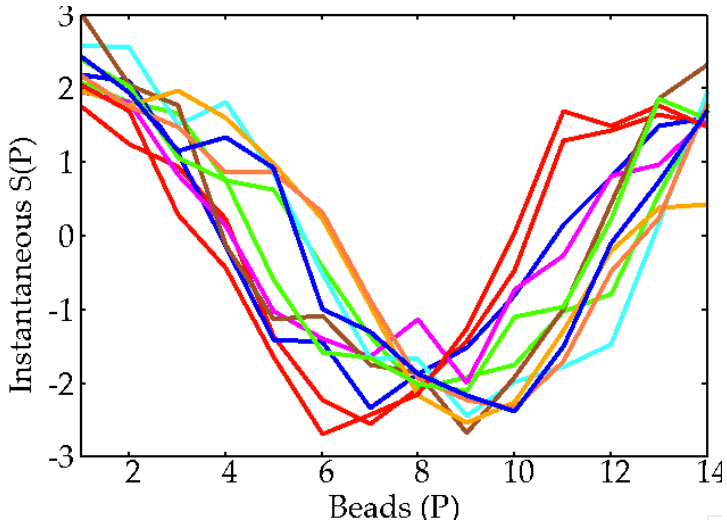

Figure 5.5: Instantaneous instanton trajectories

5.7.1 Summary

We calculated the average instanton configuration using the QBD corresponding to the MV-RPMD Hamiltonian discussed throughout this study. While the average instanton is in reasonable agreement with the exact calculation reported by Cao and Voth [4], we find the average minimum value of the instanton path to be slightly greater than the reported figure. We attribute this to an artifact of the our averaging algorithm. Our choice to make the first bead the most positive, while reordering the remaining beads contiguously causes an artificial

shift in the beads assigned to the minimum value of instantaneous paths. We see this from analyzing instantaneous instanton trajectories. While the instantaneous instanton paths have the correct minimum value, there is an ambiguity in which beads gets assigned the minimum values such that at any point in the Monte Carlo simulation bead 6-10 can have the minimum value while we'd expect the minimum to be located at bead 8 for a 14-bead calculation. Possible solutions to this issue may include initializing the PIMC simulation such that the RP solvent beads have the correct instanton configuration. Another possible solution is simulated annealing, where we run a PIMC simulation at a significantly higher temperature and initialize subsequent calculations with the converged high temperature RP configuration.

5.8 MF-RPMD Rate Theory

In the past MF-RPMD has been used to approximate the rate of ET in the condensed phase. It is known that because MF-RPMD approximates nuclear dynamics along a mean potential energy surface, it neglects fluctuation in electronic degrees of freedom. This approximation works well in multi-state systems with strong coupling between states. In the MF-RPMD approximation, nuclear motion occurs on an averaged potential surface. In strongly coupled systems this is precisely the case, where electronic transition between states are so rapid nuclear motion is approximately moving on an averaged surface. The MF-RPMD approximation fails when electronic and nuclear motion are on comparable timescales which corresponds to the nonadiabatic regime (weak coupling). This is due to the fact that MF-RPMD does not correctly account for fluctuations in electronic degrees of freedom and subsequently poorly approx-

imates nuclear motion. As a result, MF-RPMD has been widely ignored as a viable method for the simulation nonadiabatic charge and energy transfer processes.

A former member of our group, Jessica Duke, developed two remedies to the inaccuracies in MF-RPMD [24]. The first accounts for the fact that in MF-RPMD, the probability of forming "kink" configurations (probabilities of forming electronic transition states) are not correctly accounted for the the MF-RPMD flux-side TCF expression. By correctly accounting for electronic transition state probabilities in MF-RPMD rate calculation, ET rates across a full range of coupling strengths were accurately approximated. While modifying MF-RPMD such that it can reproduce nonadiabatic ET rates is an impressive feat, the probabilities of forming kinks are introduced in a mathematically inconsistent manner. Further, this method failed to capture ET in the inverted regime.

The second remedy was to introduce a population reaction coordinate, defined as the difference in product and reactant populations. This method resulted in the accurate rate calculation of ET across a full range of coupling strengths and in regimes outside of the normal regime. Despite this feat, MF-RPMD defined in terms of the population coordinate still failed to give quantitative agreement with FGR rate calculations in the inverted regime.

The following section outlines MV-RPMD rate theory developments which may alleviate some of the inherent issues with MF-RPMD and hopefully will lead to its application to general multi-level/multi-particle nonadiabatic systems in the condensed phase.

5.9 MV-RPMD Flux-side TCF: Solvent Reaction coordinate

The Bennett-Chandler expression for the rate constant is,

$$k = \frac{\langle \dot{\xi}_0 h(\dot{\xi}_0) \rangle_c \langle \delta(\xi_0 - \xi^\dagger) \rangle}{\langle h(\xi^\dagger - \xi_0) \rangle} \times \lim_{t \to \infty} \frac{\langle \dot{\xi}_0 h(\xi_t - \xi^\dagger) \rangle_c}{\langle \dot{\xi}_0 h(\dot{\xi}_0) \rangle_c \langle \delta(\xi_0 - \xi^\dagger) \rangle}. \tag{5.57}$$

canceling the numerator and denominator in the expression we get the rate in terms of a flux-side TCF introduced previously,

$$k = \lim_{t \to \infty} \frac{\langle \dot{\xi}_0 h(\xi_t - \xi^\dagger) \rangle_c}{\langle h(\xi^\dagger - \xi_0) \rangle} \tag{5.58}$$

The rate is defined in terms of a one-dimensional reaction coordinate ξ, where $\dot{\xi}_0$ is the velocity at $t = 0$ and $\xi^\ddagger$ is the dividing surface. Following the traditional mean field RPMD approach we define ξ as a function of the solvent polarization bead average, also called the ring polymer center of mass (COM), $\xi = \bar{R} = 1/N \sum_{\alpha=1}^{N} R_\alpha$, where the transition state, the reactant well, and the product well correspond to $\bar{R} = R^\dagger$, $\bar{R} \leq R^\dagger$, and $\bar{R} \geq R^\dagger$ respectively. The transition state $R^\dagger$ corresponds to the point of degeneracy between the two states. The rate can then be expressed as,

$$k = \lim_{t \to \infty} \frac{\langle \dot{\bar{R}}_0 h(\bar{R}_t - R^\dagger) \rangle_c}{\langle h(R^\dagger - \bar{R}_0) \rangle} \tag{5.59}$$

The rate constants calculated using the solvent polarization as the reaction coordinate, in the MF-RPMD framework, has been shown to severely overestimate the rate in the weak coupling regime [24]. This is because the rate expression neglects the probability of forming electronic transition states which is proportional to the coupling squared. This also fails to accurately capture reaction rates in the inverted regime.

In the MV-RPMD representation, unlike MF-RPMD, the statistical sampling and dynamics include explicit electronic state information, as well as the inter-

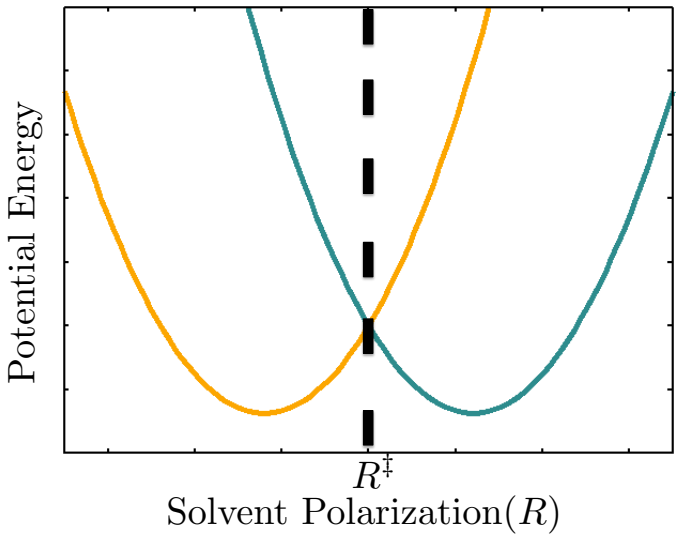

Figure 5.6: A schematic of the two-state electron transfer system in the adiabatic basis. The yellow curve is the reactant well and the green curve is the product and both are functions of solvent polarization. The black dashed line corresponds the the reaction transition state ($R^{\ddagger}$)

.

action between electronic states and nuclei in the Γ matrix defined in Eq. (2.42). Within the MV-RPMD framework the rate cate be calculated piecewise as,

$$k = \lim_{t\to\infty} \frac{\langle \dot{\bar{R}}_0 h(\bar{R}_t - R^{\dagger})\rangle_c}{\langle \mathrm{sgn}(\Theta)\rangle_c} \times \frac{\langle \mathrm{sgn}(\Theta)\rangle}{\langle h(R^{\dagger} - \bar{R}_0)\rangle} \tag{5.60}$$

where the left quantity is a dynamic calculation where initial RP configurations are sampled such that $\bar{R} = 1/N \sum_{\alpha=1}^{N} R_\alpha = 0$. Trajectories launched from this ensemble of initial configurations can be used to calculated flux-side TCF defined by the solvent polarization coordinate. The time dependent product heaviside function (left quantity in Eq. 6.15), $h(\bar{R}_t - R^{\dagger})$, is,

$$h(\bar{R}_t - R^{\dagger}) = \begin{cases} 1 \quad \text{if} \quad \bar{R}_t > 0 \quad \text{products} \\ 0 \quad \text{if} \quad \bar{R}_t < 0 \quad \text{reactants} \end{cases} \tag{5.61}$$

The static, reactant heaviside function (right quantity in Eq. 6.15) defined in

terms of solvent polarization is,

$$h(R^{\dagger} - \bar{R}_0) = \begin{cases} 1 & \text{if} \quad \bar{R}_0 < 0 \quad \text{reactants} \\ 0 & \text{if} \quad \bar{R}_0 > 0 \quad \text{products} \end{cases} \tag{5.62}$$

5.10 MV-RPMD Flux-side TCF: Population Reaction coordinate

Next we consider the reaction rate defined in terms of the population coordinate. The reaction coordinate is defined as $\xi = \Delta\mathcal{P}$, where we define $\xi = \Delta\mathcal{P}$ as the difference in bead population of the two electronic states,

$$\Delta\mathcal{P} = \begin{cases} 1 & \text{reactant} \\ 0 & \text{transition state} \\ -1 & \text{product.} \end{cases} \tag{5.63}$$

Using this reaction coordinate, the transition state, the reactant well, and the product well correspond to $\Delta\mathcal{P} = 0$, $\Delta\mathcal{P} = -1$, and $\Delta\mathcal{P} = 1$ respectively. The rate can then be expressed as,

$$k = \lim_{t\to\infty} \frac{\langle \Delta\dot{\mathcal{P}}_0 h(\Delta\mathcal{P}_t)\rangle_c}{\langle h(\Delta\mathcal{P}_0)\rangle}. \tag{5.64}$$

We run two separate simulations where we calculate,

$$\lim_{t\to\infty} \frac{\langle \Delta\dot{\mathcal{P}}_0 h(\Delta\mathcal{P}_t)\rangle_c}{\langle \mathrm{sgn}(\Theta)\rangle_c} \times \frac{\langle \mathrm{sgn}(\Theta)\rangle}{\langle h(\Delta\mathcal{P}_0)\rangle} \tag{5.65}$$

where the left quantity is a dynamic calculation where initial configurations are sampled with a constraint on the semiclassical population estimator, $\mathcal{P}_1^{\mathrm{SC}} = \mathcal{P}_2^{\mathrm{SC}} = 0.5$, for each bead in the RP. Trajectories launched from the ensemble of initial constrained configurations can be used to calculate the flux-side TCF defined by the population reaction coordinate. The population reaction coordinate

is defined in terms of the Boltzmann population as,

$$\Delta\mathcal{P} = \frac{\Gamma_2 - \Gamma_1}{\mathrm{tr}[\Gamma]} \tag{5.66}$$

The population reaction coordinate is defined in terms of the semiclassical estimator as,

$$\Delta\mathcal{P} = \mathcal{P}_2^{\mathrm{SC}} - \mathcal{P}_1^{\mathrm{SC}} \tag{5.67}$$

The derivative of the semiclassical population difference is,

$$\Delta\dot{\mathcal{P}}^{\mathrm{SC}}{}_0 = ([x_\alpha]_2[\dot{x}_\alpha]_2 + [p_\alpha]_2[\dot{p}_\alpha]_2 - [x_\alpha]_1[\dot{x}_\alpha]_1 - [p_\alpha]_1[\dot{p}_\alpha]_1). \tag{5.68}$$

and the time dependent product and static reactant heaviside functions, respectively are,

$$h(\Delta\mathcal{P}_t) = \begin{cases} 1 & \text{if} \quad \mathcal{P}_2(t) > \mathcal{P}_1(t) \\ 0 & \text{if} \quad \mathcal{P}_2(t) < \mathcal{P}_1(t) \end{cases} \tag{5.69}$$

and,

$$h(\Delta\mathcal{P}_0) = \begin{cases} 1 & \text{if} \quad \mathcal{P}_1(0) > \mathcal{P}_2(0) \\ 0 & \text{if} \quad \mathcal{P}_1(0) < \mathcal{P}_2(0) \end{cases} \tag{5.70}$$

which both can be used with the Boltzmann or semiclassical estimator.

5.11 MV-RPMD Flux-side TCF: Wigner Transform of Flux Operator

A final expression to consider is the flux-side TCF defined in terms of the Wigner transform of the flux operator in the MV-RPMD framework. We can define the rate in terms of the Wigner transformed flux operator as ,

$$k = \lim_{t\to\infty} \frac{\langle F_{\mathrm{W}}(0)\mathcal{P}_2(t)\rangle}{\langle \mathcal{P}_1(t)\rangle}. \tag{5.71}$$

We start the derivation of the Wigner transform of the flux operator by considering a two-state Hamiltonian operator defined by,

$$\hat{H} = V_{11}|1\rangle\langle 1| + V_{22}|2\rangle\langle 2| + V_{12}|1\rangle\langle 2| + V_{21}|2\rangle\langle 1| \tag{5.72}$$

$$\hat{F} = \frac{i}{\hbar}[\hat{H}, \mathcal{P}_2] \tag{5.73}$$

where,

$$\mathcal{P}_2 = |2\rangle\langle 2| \tag{5.74}$$

$$\begin{aligned}\hat{F} = \frac{i}{\hbar}(&V_{11}|1\rangle\langle 1|2\rangle\langle 2| + V_{22}|2\rangle\langle 2|2\rangle\langle 2| \\ &+V_{12}|1\rangle\langle 2|2\rangle\langle 2| + V_{21}|2\rangle\langle 1|2\rangle\langle 2| \\ &-(|2\rangle\langle 2|1\rangle\langle 1|V_{11} + |2\rangle\langle 2|2\rangle\langle 2|V_{22} \\ &+|2\rangle\langle 2|1\rangle\langle 2|V_{12} + |2\rangle\langle 2|2\rangle\langle 1|V_{21})\end{aligned} \tag{5.75}$$

since $\langle 2|1\rangle = \langle 1|2\rangle = 0$ and $\langle 2|2\rangle = \langle 1|1\rangle = 1$ we have,

$$\hat{F} = \frac{i}{\hbar}(V_{12}|1\rangle\langle 2| - V_{21}|2\rangle\langle 1|) \tag{5.76}$$

if we map discrete states to creation and annihilation operators such that $a_n^\dagger a_m = |n\rangle\langle m|$ we have,

$$\hat{F} = a_1^\dagger a_2 V_{12} - a_2^\dagger a_1 V_{21} \tag{5.77}$$

and if we note that $a_n^\dagger = \frac{1}{\sqrt{2}}(\hat{x}_n - i\hat{p}_n)$ and $a_m = \frac{1}{\sqrt{2}}(\hat{x}_m + i\hat{p}_m)$ and if we consider systems where $V_{12} = V_{21}$ we get 8 terms in the flux expression,

$$\hat{F} = \frac{i}{2\hbar}[(\hat{x}_1 - i\hat{p}_1)(\hat{x}_2 + i\hat{p}_2)V_{12} - (\hat{x}_2 - i\hat{p}_2)(\hat{x}_1 + i\hat{p}_1)V_{12}] \tag{5.78}$$

and expanding we get,

$$\begin{aligned}\hat{F} = \frac{i}{\hbar}&[V_{12}(\hat{x}_1\hat{x}_2 - i\hat{p}_1\hat{x}_2 + i\hat{x}_1\hat{p}_2 - i^2\hat{p}_1\hat{p}_2) \\ &-V_{12}(\hat{x}_2\hat{x}_1 - i\hat{p}_2\hat{x}_1 + i\hat{x}_1\hat{p}_2 - i^2\hat{p}_2\hat{p}_1)] \\ &= \frac{1}{\hbar}V_{12}(\hat{p}_1\hat{x}_2 - \hat{x}_1\hat{p}_2)\end{aligned} \tag{5.79}$$

where the knowledge of the Wigner transform of two of the expressions gives sufficient information for the Wigner transform of the other six. Following the prescription outlined in the derivation of the semiclassical estimator [56] (See Appendix) we have,

$$\begin{aligned}[-i\hat{p}_1\hat{x}_2]_W = -i \int dp_1 \int dp_2 \int d\Delta x_1 \int d\Delta x_2 \\ \times\langle x_1 - \Delta x_1/2, x_2 - \Delta x_2/2| \\ \times\hat{p}_1\hat{x}_2|x_1 + \Delta x_1/2, x_2 + \Delta x_2/2\rangle \\ \times e^{i(p_1\Delta x_1 + p_2\Delta x_2)}\end{aligned} \tag{5.80}$$

since

$$\hat{x}_2|x_1 + \Delta x_1/2, x_2 + \Delta x_2/2\rangle = (x_2 - \Delta x_2/2)|x_1 + \Delta x_1/2, x_2 + \Delta x_2/2\rangle \tag{5.81}$$

and inserting a complete set of momentum states $\mathcal{I} = \int dp_1' \int dp_2' |p_1', p_2'\rangle\langle p_1', p_2'|$.

$$\begin{aligned}[-i\hat{p}_1\hat{x}_2]_W = -i \int dp_1' \int dp_2' \int d\Delta x_1 \int d\Delta x_2 (x_2 - \Delta x_2/2) \\ \times \quad \langle x_1 - \Delta x_1/2, x_2 - \Delta x_2/2|\hat{p}_1|p_1', p_2'\rangle \\ \times\langle p_1', p_2'|x_1 + \Delta x_1/2, x_2 + \Delta x_2/2\rangle \\ \times e^{i(p_1\Delta x_1 + p_2\Delta x_2)}\end{aligned} \tag{5.82}$$

and since,

$$\hat{p}_1|p_1', p_2'\rangle = p_1|p_1', p_2'\rangle \tag{5.83}$$

we have

$$\begin{aligned}[-i\hat{p}_1\hat{x}_2]_W = -i \int dp_1' \int dp_2' \int d\Delta x_1 \int d\Delta x_2 (x_2 - \Delta x_2/2) p_1 \\ \times \quad \langle x_1 - \Delta x_1/2, x_2 - \Delta x_2/2|p_1', p_2'\rangle \\ \times\langle p_1', p_2'|x_1 + \Delta x_1/2, x_2 + \Delta x_2/2\rangle \\ \times e^{i(p_1\Delta x_1 + p_2\Delta x_2)}\end{aligned} \tag{5.84}$$

and noting

$$\langle x_1 - \Delta x_1/2, x_2 - \Delta x_2/2 | p_1', p_2' \rangle = e^{ip_1'(x_1+\Delta x_1/2)} e^{ip_2'(x_2+\Delta x_2/2)} \tag{5.85}$$

we get,

$$[-i\hat{p}_1\hat{x}_2]_W = -i \int dp_1' \int dp_2' \int d\Delta x_1 \int d\Delta x_2 (x_2 - \Delta x_2/2) p_1 \tag{5.86}$$

$$\times e^{ip_1'(x_1+\Delta x_1/2)} e^{ip_2'(x_2+\Delta x_2/2)}$$

$$\times e^{-ip_1'(x_1-\Delta x_1/2)} e^{-ip_2'(x_2-\Delta x_2/2)}$$

$$\times e^{i(p_1\Delta x_1 + p_2\Delta x_2)}$$

(5.87)

and using the definition in Eq. (A.11) we find,

$$[-i\hat{p}_1\hat{x}_2]_W = -i \int dp_1' \int dp_2' \int d\Delta x_1 \int d\Delta x_2 (x_2 - \Delta x_2/2) p_1 \tag{5.88}$$

$$\times e^{ip_1'\Delta x_1} e^{ip_2'\Delta x_2}$$

$$\times e^{i(p_1\Delta x_1 + p_2\Delta x_2)}$$

$$= \int d\Delta x_1 \int d\Delta x_2 (x_2 - \Delta x_2/2) p_1$$

$$\times \delta(\Delta x_1)\delta(\Delta x_2)$$

$$\times e^{i(p_1\Delta x_1 + p_2\Delta x_2)} = -ip_1 x_2$$

so we have,

$$[-i\hat{p}_1\hat{x}_2]_W = -ip_1 x_2 \tag{5.89}$$

Thus we have a continuous expression for the flux in terms of conjugate variables,

$$[\hat{F}]_W = \frac{1}{\hbar}[V_{12}(p_1 x_2 - x_1 p_2)]. \tag{5.90}$$

5.12 Summary

In this section we discussed limitations of MF-RPMD nonadiabatic rate calculations and why one might be interested in the formulation of an MV-RPMD rate theory. First we noted that rate calculations formulated in terms of solvent polarization COM, in the MF-RPMD formalism, do not work well at capturing nonadiabatic reaction rates. This is because constraining initial electronic population does sufficiently constrain nuclear coordinates and constraining nuclear coordinates do not sufficiently constrain population. This results in the requirement of a double constraint in population and nuclear coordinates, which proves to be numerically demanding in practice. The correction to the rate is therefore introduced by multiplying the estimator for flux-side by the probability of forming RP ”kinks” which corresponds to the probability of forming electronic transition states. While this correction to the rate calculation allowed for the use of MF-RPMD to calculate rates across a full range of coupling strengths, it is mathematically inconsistent and fails to capture ET in the inverted regime.

In an effort to remedy this inconsistency, the population difference coordinate was developed. The population coordinate distinguishes between reactants and products in all regimes of ET and gives the desired turnover for ET in the inverted regime. Still given that this method restricts kink formation outside of the adiabatic crossing, it fails to quantitatively agree with the exact FGR rate calculation.

We then sought to explore different formulations of the flux-side TCFs in the MV-RPMD formalism where ”kink” probabilities are accounted for in a mathematically consistent manner. Ideally we would like to be able to capture reac-

tion rates across a full range of coupling strengths, and across all regimes while keeping our methods general for multi-electron systems. Further, if we wish to study the rate of photochemical reactions, MV-RPMD is ideal since it consistently treats discrete system states with continuous conjugate variables.

Working toward the goal of applying MV-RPMD to a rate calculation, we explore three MV-RPMD rate formulations. The first is the MV-RPMD flux-side TCF defined in terms of a solvent polarization reaction coordinate. The second is the MV-RPMD flux-side TCF defined in terms of a population difference reaction coordinate. Finally, we outline the derivation of the continuous representation of the flux operator (for a two-state system) which can be implemented in a flux-side MV-RPMD TCF calculation. In the future we hope to apply these MV-RPMD rate theories to rate calculations in nonadiabatic condensed phase systems. This will inform the development of an efficient yet general MV-RPMD rate theory that can be applied to multi-state systems across a wide range of coupling strengths and regimes.

CHAPTER 6

CONCLUSIONS

This dissertation focused on the extension and application of a nonadiabatic version of RPMD (MV-RPMD), which allowed for the accurate and efficient simulation of quantum mechanical reactions in the condensed phase. We started our discussion with a review of imaginary-time path integrals and the classical isomorphism that falls out of the path integral discretization of the QBD. This provides an exact, yet efficient, method for generating quantum statistics for systems in the condensed phase.

Next we reviewed the real-time extension of the PI formalism, RPMD, which approximates Kubo-transformed thermal correlation functions and gives the exact result as $t \to 0$. We then went on to discuss the details of the RPMD approximations, its limitations and motivations for its extension. While RPMD has been successfully applied to a wide range of chemical problem, it's inability to treat features like quantum coherence, multi-quantum particle processes, and multi-state processes necessitates efforts toward its extension.

Our review of nonadiabatic extensions of RPMD motivated our discussion of MV-RPMD. In MV-RPMD we represent discrete system states with continuous variables by mapping to SEO states. We then take the Wigner Transform of the SEO states in order to represent our system with a quasi-probability distribution which allow us to sample continuous conjugate variables that can be integrated in classical EOMs. We also derive an improved QBD in the MV-RPMD framework by employing the symmetric Trotter splitting of kinetic and potential energy operators. We demonstrate improved numerical stability in average energy bead convergence of a model ET system.

To motivate our study of PCET using MV-RPMD, we review the model PCET systems that have been reported in the literature. The first was PCET modeled by capped Coulombic wells coupled to a proton double well in the presence of a solvent coordinate. RPMD bead convergence within this model depends on the proton and electron mass, which typically requires 32 beads and 1024 beads for converged dynamics respectively. The shortcoming of this model is its treatment of the electron and proton as unique particles. The next model studied was a proton double well coupled to discrete ET states coupled to a proton double well. Since we are working in the weak coupling (nonadiabatic) regime, the burden of bead convergence is dominated by the light proton mass, which requires 32 beads. In the MV-RPMD representation, the 32 bead requirement proves to be computationally demanding. We then turn to the method of quasi-diabatization in order to represent our PCET system with four discrete electron/proton states. This significantly reduces the number of beads required for convergence in equilibrium and dynamic simulations. We were able to demonstrate that MV-RPMD can be used to accurately distinguish between concerted and sequential PCET processes.

In order to extend our application of MV-RPMD to nonadiabatic rate calculations in the condensed phase, we review two equivalent rate theories, the flux-side thermal correlation function and the Semiclassical "ImF" method. The latter has been shown to be equivalent to RPMD rate calculations in the deep tunneling regime (where the barrier can be approximated by a harmonic well) which further shed light on the nature of the RPMD approximation. Knowing that the instanton is the imaginary-time periodic path around a reaction barrier, or the real-time path on an inverted potential barrier, we can use MV-RPMD to calculate instanton configuration by sampling configurations at the barrier. We

calculate the average instanton configuration for a two-state model in the weak coupling regime and found our preliminary results to agree qualitatively with exact calculations reported in the literature.

Finally, we reviewed RPMD rate theory, past applications and motivations for its extension. We then formulated two flux-side TCF expressions using the MV-RPMD formalism. The first involved a reaction coordinate defined by the solvent polarization COM where dynamic trajectories are initialized such that the RP solvent polarization COM is constrained to the barrier. The second involves a population coordinate defined by the difference in the product and reactant population where the propagated product heaviside can either be defined in terms of the Boltzmann or the semiclassical population estimator. Finally we provide the derivation of the flux estimator which we can use within the MV-RPMD formalism to calculate a flux-side TCF.

More recent work in our group has been toward finding the optimal dividing surface on the MV-RPMD effective potential (MV-RPMD instanton) for the calculation of nonadiabatic rates in the condensed phase [74]. The development of a robust MV-RPMD rate theory that is applicable across a full range of coupling strengths and across all regimes will further the progress toward simulating and subsequently understanding complex charge and energy processes in the condensed phase. Deeper understanding of these process will inform the rational design of novel materials in renewable energy technologies.

APPENDIX A

CHAPTER 1 OF APPENDIX

A.1 Derivation of Semiclassical Population estimator

We start the derivation of the semiclassical population estimator with the following definitions,

$$\langle x|p\rangle = \frac{1}{(2\pi)^{1/2}} e^{ipx} \tag{A.1}$$

$$\int \langle x|p\rangle\langle p|x'\rangle dp = \frac{1}{2\pi}\int e^{ip(x-x')}dp = \delta(x-x') \tag{A.2}$$

and

$$\int \delta(x) f(x) = f(0) \tag{A.3}$$

if we have the operator $\hat{S}$, for the thermal population of a particular state α, defined by

$$\hat{S} = \frac{1}{2}(\hat{x}_\alpha^2 + \hat{p}_\alpha^2 - 1) \tag{A.4}$$

the wigner transform of $\hat{S}$ is,

$$[\hat{S}]_W = \int d\Delta\mathbf{x}\langle \mathbf{x} - \Delta\mathbf{x}/\mathbf{2}|\hat{\mathbf{S}}|\mathbf{x} + \Delta\mathbf{x}/\mathbf{2}\rangle \mathbf{e}^{\mathbf{ip}\cdot\Delta\mathbf{x}} \tag{A.5}$$

if we have $\alpha = 1$, for a two-sate system

$$[\hat{x}_1^2]_W = \int d\Delta x_1 \int d\Delta x_2 \langle x_1 - \Delta x_1/2, x_2 - \Delta x_2/2|\hat{x}_1^2|x_1 + \Delta x_1/2, x_2 + \Delta x_2/2\rangle e^{i(p_1\Delta x_1 + p_2\Delta x_2)} \tag{A.6}$$

$$[\hat{x}_1^2]_W = \int d\Delta x_1 \int d\Delta x_2 (x_1 + \Delta x_1/2)^2 \delta(\Delta x_1)\delta(\Delta x_2) e^{i(p_1\Delta x_1 + p_2\Delta x_2)} = x_1^2 \tag{A.7}$$

since,

$$\langle x_\alpha - \Delta x_\alpha/2|x_\alpha + \Delta x_\alpha/2\rangle = \delta(\Delta x_\alpha) \tag{A.8}$$

$$[\hat{p}_1^2]_W = \int d\Delta x_1 \int d\Delta x_2 \langle x_1 - \Delta x_1/2, x_2 - \Delta x_2/2|\hat{p}_1^2|x_1 + \Delta x_1/2, x_2 + \Delta x_2/2\rangle e^{i(p_1\Delta x_1 + p_2\Delta x_2)} \tag{A.9}$$

and we insert a complete set of momentum states,

$$\mathcal{I} = \int dp_1' \int dp_2' |p_1', p_2'\rangle\langle p_1', p_2'| \tag{A.10}$$

$$\begin{aligned}[\hat{p}_1^2]_W = &\int dp_1' \int dp_2' \int d\Delta x_1 \int d\Delta x_2 \\ &\times \quad \langle x_1 - \Delta x_1/2, x_2 - \Delta x_2/2|\hat{p}_1^2|p_1', p_2'\rangle \\ &\times\langle p_1', p_2'|x_1 + \Delta x_1/2, x_2 + \Delta x_2/2\rangle e^{i(p_1\Delta x_1 + p_2\Delta x_2)}\end{aligned} \tag{A.11}$$

$$\begin{aligned}[\hat{p}_1^2]_W = &\int dp_1' \int dp_2' \int d\Delta x_1 \int d\Delta x_2 (p_1'^2) \\ &\times e^{ip_1'(x_1+\Delta x_1/2)} e^{ip_2'(x_2+\Delta x_2/2)} \\ &\times e^{-ip_1'(x_1-\Delta x_1/2)} e^{-ip_2'(x_2-\Delta x_2/2)} \\ &\times e^{i(p_1\Delta x_1 + p_2\Delta x_2)} \\ = &\int dp_1' \int dp_2' \int d\Delta x_1 \int d\Delta x_2 (p_1'^2) \\ &\times e^{ip_1'\Delta x_1} e^{ip_2'\Delta x_2} \\ &\times e^{i(p_1\Delta x_1 + p_2\Delta x_2)} \\ = &\int d\Delta x_1 \int d\Delta x_2 (p_1'^2) \\ &\times \delta(\Delta x_1)\delta(\Delta x_2) \\ &\times e^{i(p_1\Delta x_1 + p_2\Delta x_2) = p_1^2}\end{aligned} \tag{A.12}$$

and it's easy to show the Wigner transform of a constant is the constant itself.

$$[1]_W = \int d\Delta x_1 \int d\Delta x_2 \langle x_1 - \Delta x_1/2, x_2 - \Delta x_2/2|1|x_1 + \Delta x_1/2, x_2 + \Delta x_2/2\rangle e^{i(p_1\Delta x_1 + p_2\Delta x_2)} = 1 \tag{A.13}$$

so finally we have $[\hat{S}_\alpha]_W$ for a particular state α,

$$[\hat{S}]_W = \frac{1}{2}(x_\alpha^2 + p_\alpha^2 - 1). \tag{A.14}$$

A.2 Parameters for Quasi-Diabatic Potential Surfaces

We provide the diabatic potential energy matrix parameters for all three models below.

Diabat	a	b	c
V_{DD}	0.0015	0.0075	-0.0041
V_{DA}	0.0015	0.0055	0.0072
V_{AD}	0.0015	-0.0055	0.0072
V_{AA}	0.0015	-0.0075	-0.0041

Table A.1: Diabatic potential energy surface parameters for model I

Coupling	Δ
$V_{\mathrm{DD,DA}}$	9.7×10^{-5}
$V_{\mathrm{DD,AD}}$	2.5×10^{-3}
$V_{\mathrm{DD,AA}}$	1.8×10^{-4}
$V_{\mathrm{DA,AD}}$	1.8×10^{-4}
$V_{\mathrm{DA,AA}}$	2.5×10^{-3}
$V_{\mathrm{AD,AA}}$	9.7×10^{-5}

Table A.2: Diabatic coupling matrix elements for model I

Diabat	a	b	c
V_{DD}	0.0015	0.0072	-0.0018
V_{DA}	0.0018	0.0058	-0.0013
V_{AD}	0.0018	-0.0061	0.0034
V_{AA}	0.0016	-0.0083	-0.0018

Table A.3: Diabatic potential energy surface parameters for model II

Coupling	Δ
$V_{\mathrm{DD,DA}}$	1.1×10^{-3}
$V_{\mathrm{DD,AD}}$	1.2×10^{-4}
$V_{\mathrm{DD,AA}}$	1.2×10^{-4}
$V_{\mathrm{DA,AD}}$	1.2×10^{-4}
$V_{\mathrm{DA,AA}}$	1.2×10^{-4}
$V_{\mathrm{AD,AA}}$	1.4×10^{-3}

Table A.4: Diabatic coupling matrix elements for model II

Diabat	a	b	c
V_{DD}	0.0015	0.008	0.0009
V_{DA}	0.0015	0.0098	0.013
V_{AD}	0.0015	-0.0056	-0.0095
V_{AA}	0.0015	-0.013	0.0009

Table A.5: Diabatic potential energy surface parametersfor model III.

Coupling	Δ
$V_{\mathrm{DD,DA}}$	6.9×10^{-4}
$V_{\mathrm{DD,AD}}$	2.5×10^{-3}
$V_{\mathrm{DD,AA}}$	1.8×10^{-4}
$V_{\mathrm{DA,AD}}$	1.8×10^{-4}
$V_{\mathrm{DA,AA}}$	2.5×10^{-3}
$V_{\mathrm{AD,AA}}$	6.9×10^{-4}

Table A.6: Diabatic coupling matrix elements for model III

BIBLIOGRAPHY

[1] David Chandler and Peter G. Wolynes. Exploiting the isomorphism between quantum theory and classical statistical mechanics of polyatomic fluids. *J. Chem. Phys.*, 74:4078–4095, 1981.

[2] Nandini Ananth. Mapping variable ring polymer molecular dynamics: A path-integral based method for nonadiabatic processes. *J. Chem. Phys.*, 139(12):124102, 2013.

[3] Jeremy O. Richardson and Stuart C. Althorpe. Ring-polymer molecular dynamics rate-theory in the deep-tunneling regime: Connection with semiclassical instanton theory. *J. Chem. Phys.*, 131(214106), 2009.

[4] Jianshu Cao, Camilla Minichino, and Gregory A. Voth. The computation of electron transfer rates: The nonadiabatic instanton solution. *J. Chem. Phys.*, 103(1391), 1995.

[5] My Hang V Huynh and Thomas J Meyer. Proton-coupled electron transfer. *Chem. Rev.*, 107(11):5004–5064, 2007.

[6] R. I. Cukier and D. G. Nocera. Proton-coupled electron transfer. *Ann. Rev. Phys. Chem.*, 49(1):337–369, 1998.

[7] Sharon Hammes-Schiffer and Alexander V Soudackov. Proton-coupled electron transfer in solution, proteins, and electrochemistry. *J. Phys. Chem. B*, 112(45):14108–14123, 2008.

[8] Jeffrey J Warren, Tristan A Tronic, and James M Mayer. Thermochemistry of proton-coupled electron transfer reagents and its implications. *Chem. Rev.*, 110(12):6961–7001, 2010.

[9] Mrten Wikström. Identification of the electron transfers in cytochrome oxidase that are coupled to proton-pumping. *Nature*, 338(6218):776–778, 1989.

[10] Daniel G. Nocera. Solar fuels and solar chemicals industry. *Acc. Chem. Res.*, 50(3):616–619, 2017.

[11] Nancy Makri. Time-dependent quantum methods for large systems. *Annu. Rev. Phys. Chem.*, 50:167–191, 1999.

[12] Sharon Hammes-Schiffer and Alexei A Stuchebrukhov. Theory of coupled electron and proton transfer reactions. *Chem. Rev.*, 110(12):6939–6960, 2010.

[13] Sharon Hammes-Schiffer. Proton-coupled electron transfer: Moving together and charging forward. *J. Am. Chem. Soc.*, 137(28):8860–8871, 2015.

[14] S. Habershon, D. E. Manolopoulos, T. E. Markland, and :T. F. Miller III. Ring-polymer molecular dynamics: quantum effects in chemical dynamics from classical trajectories in an extended phase space. *Ann. Rev. Phys. Chem.*, 64:387–413, 2013.

[15] Thomas F. Miller III and David E. Manolopoulos. Quantum diffusion in liquid para-hydrogen from ring-polymer molecular dynamics. *J. Chem. Phys.*, 122(184503), 2005.

[16] Nicholas Boekelheide, Romelia Salomon-Ferrer, and Thomas F. Miller, III. Dynamics and dissipation in enzyme catalysis. *Proc. Natl. Acad. Sci. U.S.A*, 108:16159–16163, 2011.

[17] Yury V. Suleimanova, Rosana Collepardo-Guevara, and David E. Manolopoulos. Bimolecular reaction rates from ring polymer molecular dynamics: Application to $H + CH_4 \rightarrow H_2 + CH_3$. *J. Chem. Phys.*, 134(044131), 2011.

[18] Rosana Collepardo-Guevara, Yury V. Suleimanov, and David E. Manolopoulos. Bimolecular reaction rates from ring polymer molecular dynamics. *J. Phys. Chem.*, 130(174713), 2009.

[19] Artur R Menzeleev, Nandini Ananth, and Thomas F Miller III. Direct simulation of electron transfer using ring polymer molecular dynamics: Comparison with semiclassical instanton theory and exact quantum methods. *J. Chem. Phys.*, 135(7):074106, 2011.

[20] Kenion Rachel L. and Nandini Ananth. Direct simulation of electron transfer in the cobalt hexammine(ii/iii) self-exchange reaction. *Phys.Chem.Chem.Phys.*, 18(26117), 2016.

[21] Farnaz A. Shakib and Pengfei Huo. Ring polymer surface hopping: Incorporating nuclear quantum effects into nonadiabatic molecular dynamics simulations. *J. Chem. Phys.*, 8(13):3073–3080, 2017.

[22] Artur R. Menzeleev, Franziska Bell, and Thomas F. Miller III. Kinetically

constrained ring-polymer molecular dynamics for non-adiabatic chemical reactions. *J. Chem. Phys.*, 140(6), 2014.

[23] Sutirtha N. Chowdhury and Pengfei Huo. Coherent state mapping ring polymer molecular dynamics for non-adiabatic quantum propagations. *J. Chem. Phys.*, 147(214109), 2017.

[24] Jessica R. Duke and Nandini Ananth. Mean field ring polymer molecular dynamics for electronically nonadiabatic reaction rates. *Faraday Discuss.*, 195, 2016.

[25] Philip Shushkov, Richard Li, and John C. Tully. Ring polymer molecular dynamics with surface hopping. *The Journal of Chemical Physics*, 137(22):22A549, Dec 2012.

[26] Jeremy O. Richardson and Michael Thoss. Communication: Nonadiabatic ring-polymer molecular dynamics. *J. Chem. Phys.*, 139(3):031102, 2013.

[27] Jessica R. Duke and Nandini Ananth. Simulating excited state dynamics in systems with multiple avoided crossings using mapping variable ring polymer molecular dynamics. *J. Phys. Chem. Lett.*, 6(21):4219–4223, 2015.

[28] Sadrach Pierre, Jessica R. Duke, T. J. H. Hele, and Nandini Ananth. A mapping variable ring polymer molecular dynamics study of condensed phase proton-coupled electron transfer. *J. Chem. Phys.*, 147(2017), 2017.

[29] Dmitrii E. Makarov and Nancy Makri. Path integrals for dissipative systems by tensor multiplication. condensed phase quantum dynamics for arbitrarily long time. *Chem. Phys. Lett.*, 221:482–491, 1994.

[30] Nancy Makri. Numerical path integral techniques for long time dynamics of quantum dissipative systems. *J. Math. Phys.*, 35(5):2430, 1995.

[31] Richard P. Feynman and Albert R. Hibbs. *Quantum Mechanics and Path Integrals*. McGraw-Hill, New York, 1965.

[32] M. Parrinello and A. Rahman. Study of an f center in molten kcl study of an f center in molten kcl study of an f center in molten kcl study of an f cent in molten kcl. *J. Chem. Phys.*, 80:860, 1984.

[33] David Chandler and Peter G. Wolynes. Exploiting the isomorphism be-

tween quantum theory and classical statistical mechanics of polyatomic fluids. *J. Chem. Phys.*, 74:4078, 1981.

[34] M. E. Tuckerman and A. Hughes. *Classical and Quantum Dynamics in Condensed Phase Simulations*. World Scientific, Singapore, 1998.

[35] Maria Topaler and Nancy Makri. Quantum rates for a double well coupled to a dissipative bath: Accurate path integral results and comparison with approximate theories. *J. Chem. Phys.*, 101:7500–7519, 1994.

[36] Aaron Kelly, Andrés Montoya-Castillo, Lu Wang, and Thomas E. Markland. Generalized quantum master equations in and out of equilibrium: when can one win? *J. Chem. Phys.*, 144:184105, 2016.

[37] Aaron Kelly, Nora Brackbill, and Thomas E. Markland. Accurate nonadiabatic quantum dynamics on the cheap: Making the most of mean field theory with master equations. *J. Chem. Phys.*, 142:094110, 2015.

[38] Bastiaan J. Braams and David E. Manolopoulos. On the short-time limit of ring polymer molecular dynamics. *J. Chem. Phys.*, 125(124105), 2006.

[39] Ian R. Craig and David E. Manolopoulos. Quantum statistics and classical mechanics: Real time correlation functions from ring polymer molecular dynamics. *J. Chem. Phys.*, 121(8):3368–3373, 2004.

[40] Stuart C. Althorpe and Timothy J. H. Hele. Derivation of a true ($t \rightarrow 0_+$) quantum transition-state theory. i. uniqueness and equivalence to ring-polymer molecular dynamics transition-state-theory. *J. Chem. Phys.*, 138:084108, 2013.

[41] Stuart C. Althorpe and Timothy J. H. Hele. Derivation of a true ($t \rightarrow 0_+$) quantum transition-state theory. ii. recovery of the exact quantum rate in the absence of recrossing. *J. Chem. Phys.*, 139(8):084115, 2013.

[42] T. J. H. Hele, M. J. Willatt, A. Muolo, and S. C. Althorpe. Boltzmann-conserving classical dynamics in quantum time-correlation functions: 'matsubara dynamics'. *J. Chem. Phys.*, 142:134103, 2015.

[43] T. J. H. Hele, M. J. Willatt, A. Muolo, and S. C. Althorpe. Communication: Relation of centroid molecular dynamics and ring-polymer molecular dynamics to exact quantum dynamics. *J. Chem. Phys.*, 142:191101, 2015.

[44] Artur R. Menzeleev, Nandini Ananth, and Thomas F. Miller III. Direct simulation of electron transfer using ring polymer molecular dynamics: Comparison with semiclassical instanton theory and exact quantum methods. *J. Chem. Phys.*, 135(7), 2011.

[45] Rosana Collepardo-Guevara, Ian R. Craig, and David E. Manolopoulos. Proton transfer in a polar solvent from ring polymer reaction rate theory. *J. Chem. Phys.*, 128:144502, 2008.

[46] Joshua S. Kretchmer and Thomas F. Miller, III. Kinetically-constrained ring-polymer molecular dynamics for non-adiabatic chemistries involving solvent and donor-acceptor dynamical effects. *Farad. Discuss.*,, 195:191–214, 2016.

[47] Shinichi Miura and Susumu Okazaki. Path integral molecular dynamics for bose–einstein and fermi–dirac statistics. *J. Chem. Phys.*, 112(23):Okazaki2000, 2000.

[48] Militzer B. and D. M. Ceperley. Path integral monte carlo calculation of the deuterium hugoniot. *Phys. Rev. Lett.*, 85(9):1890, 2000.

[49] Michael Thoss and Gerhard Stock. Mapping approach to the semiclassical description of nonadiabatic quantum dynamics. *Phys. Rev. A*, 59:64–79, Jan 1999.

[50] Joshua S. Kretchmer and Thomas F. Miller III. Tipping the balance between concerted versus sequential proton-coupled electron transfer. *Inorg. Chem.*, 55(3):1022–1031, 2016.

[51] Joshua S. Kretchmer and Thomas F. Miller III. Direct simulation of proton-coupled electron transfer across multiple regimes. *J. Chem. Phys.*, 138(13), 2013.

[52] Jian-Yun Fang and Sharon Hammes-Schiffer. Proton-coupled electron transfer reactions in solution: Molecular dynamics with quantum transitions for model systems. *J. Chem. Phys.*, 106(20):8442–8454, 1997.

[53] Nandini Ananth and Thomas F. Miller III. Flux-correlation approach to characterizing reaction pathways in quantum systems: a study of condensed-phase proton-coupled electron transfer. *Mol. Phys.*, 110(9-10):1009–1015, 2012.

[54] A.O Caldeira and A.J Leggett. Quantum tunnelling in a dissipative system. *Ann. Phys.*, 149(2):374 – 456, 1983.

[55] Ian R. Craig and David E. Manolopoulos. A refined ring polymer molecular dynamics theory of chemical reaction rates. *J. Chem. Phys.*, 123(3):034102, 2005.

[56] Timothy J. H. Hele and Nandini Ananth. Deriving the exact nonadiabatic quantum propagator in the mapping variable representation. *Faraday Discuss.*, 195:269–289, 2016.

[57] Hans-Dieter Meyer and William H. Miller. A classical analog for electronic degrees of freedom in nonadiabatic collision processes. *J. Chem. Phys.*, 70(7):3214–3223, 1979.

[58] Gerhard Stock and Michael Thoss. Semiclassical description of nonadiabatic quantum dynamics. *Phys. Rev. Lett.*, 78:578–581, Jan 1997.

[59] Jeremy O. Richardson, Philipp Meyer, Marc-Oliver Pleinert, and Michael Thoss. An analysis of nonadiabatic ring-polymer molecular dynamics and its application to vibronic spectra. *Chem. Phys.*, 482:124–134, 2017.

[60] Enrico Fermi. *Nuclear physics: a course given by Enrico Fermi at the University of Chicago, (University of Chicago Press, 1950)*.

[61] Niels E Henriksen and Flemming Y Hansen. *Theories of molecular reaction dynamics: the microscopic foundation of chemical kinetics, (Oxford University Press on Demand, 2008)*.

[62] Jens Ulstrup and Joshua Jortner. The effect of intramolecular quantum modes on free energy relationships for electron transfer reactions. *J. Chem. Phys.*, 63(10):4358–4368, 1975.

[63] Nancy Makri. Stabilization of localized states in dissipative tunneling systems interacting with monochromatic fields. *J. Chem. Phys.*, 106(6):2286–2297, 1997.

[64] William H. Miller. Quantum mechanical transition state theory and a new semiclassical model for reaction rate constants. *J. Chem. Phys.*, 61:1823, 1974.

[65] William H. Miller, Steven D. Schwartz, and John W. Tromp. Quantum mechanical rate constants for bimolecular reactions. *J. Chem. Phys.*, 79:4889, 1983.

[66] L. I. Schiff. *Quantum Mechanics*. McGraw-Hill, New York, 1968.

[67] Ian R. Craig and David E. Manolopoulos. Chemical reaction rates from ring polymer molecular dynamics. *J. Chem. Phys.*, 122:084106, 2004.

[68] Haobin Wang, Xiong Sun, and William H. Miller. Semiclassical approximations for the calculation of thermal rate constants for chemical reactions in complex molecular systems. *J. Chem. Phys.*, 108:9726, 1998.

[69] Xiong Sun, Haobin Wang, and William H. Miller. Semiclassical theory of electronically nonadiabatic dynamics: Results of a linearized approximation to the initial value representation. *J. Chem. Phys.*, 109:7064, 1998.

[70] Eitan Geva and Qiang Shi. Quantum-mechanical reaction rate constants from centroid molecular dynamics simulations. *J. Chem. Phys.*, 115:9209, 2001.

[71] Ian Affleck. Quantum-statitical metastability. *Phys. Rev. Lett.*, 46(6):388, 1981.

[72] Curtis G. Callan, Jr. and Sidney Coleman. Fate of the false vacuum. ii. first quantum corrections*. *Phys. Rev. D*, 16(6):1762, 1977.

[73] V. A. Benderkii, Dmitrii E. Makarov, and C.A. Wight. *Advance in Chemical Physics, Volume LXXXVIII*. John Wiley and Sons, 1994.

[74] Srinanth Ranya, Sadrach Pierre, and Nandini Ananth. Optimal dividing surfaces for nonadiabatic rate calculations using the mapping variable coordinate space instanton. *Manuscript in preparation*, 2018.